

AD-A195 997

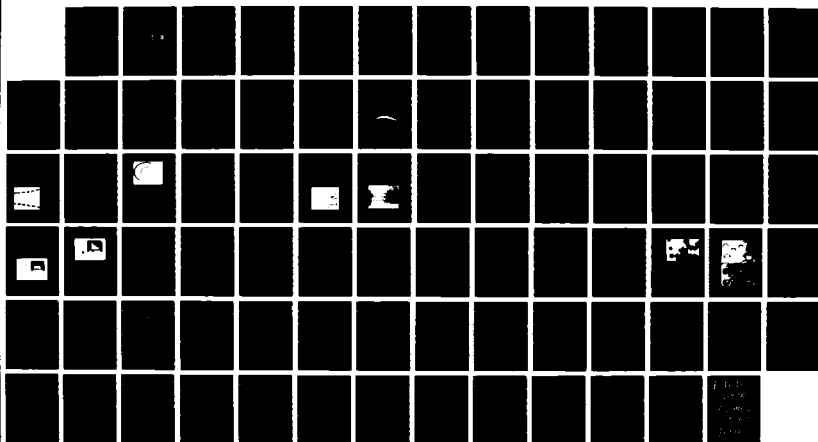
VOLUMETRIC MEASUREMENT OF VORTICITY VECTORS BY OPTICAL 1/1  
PROBE(U) PHYSICAL SCIENCES INC ANDOVER MA  
R D FERGUSON ET AL. 27 MAY 88 PSI-1848/TR-795

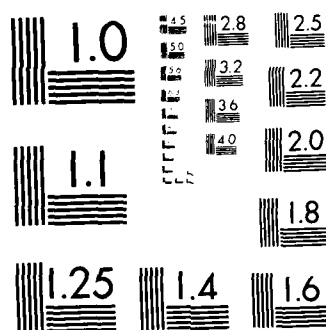
UNCLASSIFIED

N00014-87-C-0065

F/G 14/2

NL





MICROCOPY RESOLUTION TEST CHART  
NATIONAL BUREAU OF STANDARDS 1963-A

DTIC FILE COPY

4

AD-A195 997

TR-795

VOLUMETRIC MEASUREMENT OF VORTICITY  
VECTORS BY OPTICAL PROBE

D. Ferguson  
M. Frish

Physical Sciences Inc.  
Research Park, Box 3100  
Andover, MA 01810

27 May 1988

Final Report

Prepared for:

Office of Naval Research  
800 N. Quincy Street  
Arlington, VA 22217-5000

Contract No. N00014-87-C-0865

DTIC  
ELECTE  
JUN 21 1988  
S D  
O&D

**DISTRIBUTION STATEMENT A**

Approved for public release  
Distribution Unlimited

UNCLASSIFIED

SECURITY CLASSIFICATION OF THIS PAGE

## REPORT DOCUMENTATION PAGE

1. REPORT SECURITY CLASSIFICATION UNCLASSIFIED			1b. RESTRICTIVE MARKINGS	
2. SECURITY CLASSIFICATION AUTHORITY			3. DISTRIBUTION / AVAILABILITY OF REPORT	
3. DECLASSIFICATION / DOWNGRADING SCHEDULE				
4. PERFORMING ORGANIZATION REPORT NUMBER(S) PSI-1048/TR-795			5. MONITORING ORGANIZATION REPORT NUMBER(S)	
6a. NAME OF PERFORMING ORGANIZATION Physical Sciences Inc.		6b. OFFICE SYMBOL (If applicable)	7a. NAME OF MONITORING ORGANIZATION Office of Naval Research	
6c. ADDRESS (City, State, and ZIP Code) Research Park, Box 3100 Andover, MA 01810			7b. ADDRESS (City, State, and ZIP Code) Department of the Navy 800 N. Quincy St. Arlington, VA 22217-5000	
8a. NAME OF FUNDING / SPONSORING ORGANIZATION Office of Naval Research		8b. OFFICE SYMBOL (If applicable)	9. PROCUREMENT INSTRUMENT IDENTIFICATION NUMBER N00014-87-C-0865	
10. SOURCE OF FUNDING NUMBERS				
10a. ADDRESS (City, State, and ZIP Code) Department of the Navy 800 N. Quincy St. Arlington, VA 22217-5000			PROGRAM ELEMENT NO.	PROJECT NO.
			TASK NO.	WORK UNIT ACCESSION NO.
11. TITLE (Include Security Classification) VOLUMETRIC MEASUREMENT OF VORTICITY VECTORS BY OPTICAL PROBE				
12. PERSONAL AUTHOR(S) R. Daniel Ferguson and Michael B. Frish				
13a. TYPE OF REPORT FINAL		13b. TIME COVERED FROM 9/87 TO 3/88		14. DATE OF REPORT (Year, Month, Day) 1988 May 27
15. PAGE COUNT				
16. SUPPLEMENTARY NOTATION				
17. COSATI CODES			18. SUBJECT TERMS (Continue on reverse if necessary and identify by block number)	
FIELD	GROUP	SUB-GROUP		
19. ABSTRACT (Continue on reverse if necessary and identify by block number)  The general goal of this Phase I SBIR Program was to demonstrate that the fluid flow measurement technique known as the Vorticity Optical Probe (VOP), could be used to measure the vorticity vectors within a volume of a flow field at many distinguishable locations simultaneously. The specific objectives of the program were to demonstrate that: 1) The VOP provides sufficient information to allow rapid measurement of all three components of the vorticity vector at a single well-defined point within the flow field; 2) The vorticity vectors at several spatially distinct but unknown positions can be measured concurrently; and 3) A method could be developed for determining where in the sampling volume the vorticity is being measured. These three specific goals have been met using simulations of both the VOP and rotational flow.				
20. DISTRIBUTION / AVAILABILITY OF ABSTRACT <input type="checkbox"/> UNCLASSIFIED/UNLIMITED <input type="checkbox"/> SAME AS RPT <input type="checkbox"/> DTIC USERS			21. ABSTRACT SECURITY CLASSIFICATION	
22a. NAME OF RESPONSIBLE INDIVIDUAL			22b. TELEPHONE (Include Area Code)	22c. OFFICE SYMBOL

UNCLASSIFIED

SECURITY CLASSIFICATION OF THIS PAGE

UNCLASSIFIED

SECURITY CLASSIFICATION OF THIS PAGE

## PREFACE

This report describes the work performed at Physical Sciences Inc. (PSI) as a Phase I Small Business Innovative Research (SBIR) program sponsored by the Office of Naval Research. The general goal of the program was to demonstrate that the fluid flow measurement technique known as the Vorticity Optical Probe (VOP) could be used to measure the vorticity vectors within a volume of a flow field at many distinguishable locations simultaneously. The spatial resolution of the measurements would be small enough for them to be sensitive to the fine-scale fluctuations of the flow, yet the overall sampling volume large enough to enable study of the interactions between fine-scale features and large-scale structures. The specific objectives of the program were to demonstrate that: 1) The VOP provides sufficient information to allow rapid measurement of all three components of the vorticity vector at a single well-defined point within the flow field; 2) The vorticity vectors at several spatially distinct but unknown positions can be measured concurrently; and 3) A method could be developed for determining where in the sampling volume the vorticity is being measured.

These three specific goals have been met using simulations of both the VOP and rotational flow. A data analysis technique has been developed which demonstrates the three-component measurement capability and indicates the inherent limits on its precision. The capability to obtain vorticity data from many points simultaneously has been demonstrated, and it was found that there is a correlation between the accuracy of the vorticity measurement and the precision with which the location of the measurement within the large sampled volume is known. In this Phase I program we have shown, as planned, that one of the three position coordinates needed to pinpoint the measurement location can be easily determined, and that the other two can in principle be found by a conceptually straightforward extension of the one-coordinate technique. We have also conceived some other position measurement methods that we were

unable to pursue in Phase I but believe will ultimately be relatively easy to incorporate into a volumetric VOP system.

The remainder of this report describes the details of these accomplishments. Section 1 is primarily an introductory section which includes the background information needed for comprehension of subsequent material. Section 2 presents the Phase I work and the specific tasks which were performed to meet the objectives listed above. The report concludes with a brief discussion of the hurdles which we would intend to overcome in a Phase II program leading to commercialization of the VOP.

## ACKNOWLEDGMENTS

This work was funded by the Office of Naval Research through Contract No. N00014-87-C-0865. The authors are grateful to Dr. Spiro Lekoudis and Dr. Michael Reischman for their support and interest in the Vorticity Optical Probe.

1. per lti  
 2. per lti  
 3. per lti  
 4. per lti  
 5. per lti  
 6. per lti  
 7. per lti  
 8. per lti  
 9. per lti  
 10. per lti  
 11. per lti  
 12. per lti  
 13. per lti  
 14. per lti  
 15. per lti  
 16. per lti  
 17. per lti  
 18. per lti  
 19. per lti  
 20. per lti  
 21. per lti  
 22. per lti  
 23. per lti  
 24. per lti  
 25. per lti  
 26. per lti  
 27. per lti  
 28. per lti  
 29. per lti  
 30. per lti  
 31. per lti  
 32. per lti  
 33. per lti  
 34. per lti  
 35. per lti  
 36. per lti  
 37. per lti  
 38. per lti  
 39. per lti  
 40. per lti  
 41. per lti  
 42. per lti  
 43. per lti  
 44. per lti  
 45. per lti  
 46. per lti  
 47. per lti  
 48. per lti  
 49. per lti  
 50. per lti  
 51. per lti  
 52. per lti  
 53. per lti  
 54. per lti  
 55. per lti  
 56. per lti  
 57. per lti  
 58. per lti  
 59. per lti  
 60. per lti  
 61. per lti  
 62. per lti  
 63. per lti  
 64. per lti  
 65. per lti  
 66. per lti  
 67. per lti  
 68. per lti  
 69. per lti  
 70. per lti  
 71. per lti  
 72. per lti  
 73. per lti  
 74. per lti  
 75. per lti  
 76. per lti  
 77. per lti  
 78. per lti  
 79. per lti  
 80. per lti  
 81. per lti  
 82. per lti  
 83. per lti  
 84. per lti  
 85. per lti  
 86. per lti  
 87. per lti  
 88. per lti  
 89. per lti  
 90. per lti  
 91. per lti  
 92. per lti  
 93. per lti  
 94. per lti  
 95. per lti  
 96. per lti  
 97. per lti  
 98. per lti  
 99. per lti  
 100. per lti  
 101. per lti  
 102. per lti  
 103. per lti  
 104. per lti  
 105. per lti  
 106. per lti  
 107. per lti  
 108. per lti  
 109. per lti  
 110. per lti  
 111. per lti  
 112. per lti  
 113. per lti  
 114. per lti  
 115. per lti  
 116. per lti  
 117. per lti  
 118. per lti  
 119. per lti  
 120. per lti  
 121. per lti  
 122. per lti  
 123. per lti  
 124. per lti  
 125. per lti  
 126. per lti  
 127. per lti  
 128. per lti  
 129. per lti  
 130. per lti  
 131. per lti  
 132. per lti  
 133. per lti  
 134. per lti  
 135. per lti  
 136. per lti  
 137. per lti  
 138. per lti  
 139. per lti  
 140. per lti  
 141. per lti  
 142. per lti  
 143. per lti  
 144. per lti  
 145. per lti  
 146. per lti  
 147. per lti  
 148. per lti  
 149. per lti  
 150. per lti  
 151. per lti  
 152. per lti  
 153. per lti  
 154. per lti  
 155. per lti  
 156. per lti  
 157. per lti  
 158. per lti  
 159. per lti  
 160. per lti  
 161. per lti  
 162. per lti  
 163. per lti  
 164. per lti  
 165. per lti  
 166. per lti  
 167. per lti  
 168. per lti  
 169. per lti  
 170. per lti  
 171. per lti  
 172. per lti  
 173. per lti  
 174. per lti  
 175. per lti  
 176. per lti  
 177. per lti  
 178. per lti  
 179. per lti  
 180. per lti  
 181. per lti  
 182. per lti  
 183. per lti  
 184. per lti  
 185. per lti  
 186. per lti  
 187. per lti  
 188. per lti  
 189. per lti  
 190. per lti  
 191. per lti  
 192. per lti  
 193. per lti  
 194. per lti  
 195. per lti  
 196. per lti  
 197. per lti  
 198. per lti  
 199. per lti  
 200. per lti  
 201. per lti  
 202. per lti  
 203. per lti  
 204. per lti  
 205. per lti  
 206. per lti  
 207. per lti  
 208. per lti  
 209. per lti  
 210. per lti  
 211. per lti  
 212. per lti  
 213. per lti  
 214. per lti  
 215. per lti  
 216. per lti  
 217. per lti  
 218. per lti  
 219. per lti  
 220. per lti  
 221. per lti  
 222. per lti  
 223. per lti  
 224. per lti  
 225. per lti  
 226. per lti  
 227. per lti  
 228. per lti  
 229. per lti  
 230. per lti  
 231. per lti  
 232. per lti  
 233. per lti  
 234. <



## CONTENTS

<u>Section</u>		<u>Page</u>
1.	VOP FUNDAMENTALS	1
1.1	INTRODUCTION	1
1.2	THE VOP	2
1.2.1	VOP Geometry	3
1.2.2	Trajectory Simulations	7
1.3	PREVIOUS WORK	10
2.	PHASE I PROGRAM	13
2.1	TASK 1 - THREE COMPONENT VORTICITY MEASUREMENT	13
2.1.1	Apparatus	13
2.1.2	Data Analysis	15
2.1.3	Measurements and Results	16
2.1.4	Error Analysis	18
2.2	TASK 2 - MULTIPLE TRAJECTORIES	20
2.2.1	Apparatus	21
2.2.2	Stationary Reflections	22
2.2.3	Task 2 Results - The rotating rod	23
2.2.4	Task 2 Discussion	25
2.3	TASK 3 LOCATING REFLECTION ORIGINS	27
2.3.1	Task 3 Approach	27
2.3.2	Apparatus	28
2.3.3	Experimental Procedure	30
2.3.4	Task 3 Results	32
2.4	CONCLUSIONS	34

## FIGURES

<u>Figure</u>		<u>Page</u>
1	Illustration of trajectory along a spherical surface of reflection from a mirror rotating with vorticity $\vec{\omega}$ .	3
2	Coordinate system for analysis of reflection trajectory.	4
3	Simulated reflection trajectory families over flat 1 sr solid angle surface.	8
4	Original VOP Optical detection system.	10
5	Second generation optical system for two-component vorticity measurement (from ref 6).	12
6	The rotating mirror.	14
7	Photograph of two trajectories at different mirror pitches; $\theta_s = 20^\circ$ , $\phi_s = 144^\circ$ .	17
8	Photograph of trajectories; $\theta_s = 90^\circ$ , $\phi_s = 135^\circ$ .	19
9	Task 2 apparatus for multiple trajectory photographs.	21
10	Photograph of reflections from lead carbonate mirrors embedded in the (stationary) PMMA rod.	22
11	Trajectories of reflections from mirrors within the rotating PMMA rod.	23
12	Effects of refraction in air gap.	26
13	Coincident beams of different color or polarization.	27
14	Task 3 optical configuration for intensity gradient position measurement.	29

# FIGURES (Continued)

<u>Figure</u>		<u>Page</u>
15	False color enhanced video display of gradient "up" frame background subtracted after division by the corresponding "down" frame within the rectangular area on the reflection at upper left.	31
16	Calibration band.	32
17	Comparison of intensity gradient method and direct measurement of z-position.	33
18	Coincidence method for complete vorticity and velocity determination.	35

## TABLES

<u>Table</u>		<u>Page</u>
1	Vorticity components calculated from trajectories in Figure 7.	18
2	Vorticity components calculated from trajectories in Figure 8.	19
3	Vorticity components calculated from photo trajectories A-M.	24

## 1. VOP FUNDAMENTALS

### 1.1 INTRODUCTION

Experimental fluid mechanics, can be roughly divided into two areas; (1) Flow visualization (volumetric) experiments, wherein large volumes of a flow field are marked by dyes, smoke or other inhomogeneities, photographed, and interpreted by eye, and (2) Probes of properties at discrete points (principally anemometry). Flow visualization has been successful in educing gross features of coherent structures, but yields little quantitative information. In contrast, anemometry provides quantitative information at many scales and, with clever averaging procedures, can describe some aspects of characteristic large scale flow structures and their effects on the surrounding flow field.

Several efforts have been made to derive quantitative information from sophisticated flow visualization apparatus, but the data analysis requirements overwhelm even the largest computers.<sup>1</sup> Unfortunately, even the most exacting measurements have been unable to achieve sufficient local detail over large enough flow volumes to show the interaction, if any, of large and small scale structure. Conditional averaging procedures<sup>2</sup> for continuous measurements at discrete points necessarily filter out information in all but a narrow band of large length scales.

Quantitative volumetric measurements of flow properties over a broad range of length scales are sorely needed to advance our understanding of complex flows and ultimately develop the ability to alter and control them. Specifically, techniques are required that offer sufficient spatial resolution to distinguish fine scale motions over a sufficiently large volume to determine how the fine-scale features interact to form large scale structures, or how the fine scales are formed by interactions of the large scale structures within the mean flow.

The essential distinction between the two areas of experimental fluid dynamics, flow visualization and discrete fixed probes, is that the first is an attempt to follow the motion of many (marked) fluid elements, and the second measures some property of the flow as it convects past fixed points; Lagrangian and Eulerian respectively. Few experimental techniques fall into the middle ground of this global division. As described below, the volumetric Vorticity Optical Probe would be such a technique. The individual probe particles are passive co-moving markers of the flow field, but at the same time, they are active probes of the local vorticity vector and offer a fine intrinsic spatial resolution of  $\sim 25 \mu\text{m}$ . The complementary nature of the data thus obtained, with appropriate analysis, can potentially provide more information about the structure of the sampled flow than comparable volumes of vorticity or velocity data alone.

## 1.2 THE VOP

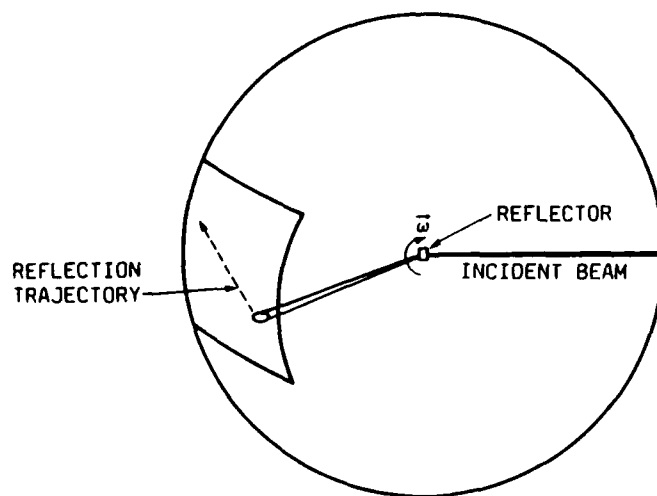
Appendix A is a copy of a published paper which provides the essential details of the technique recently developed by Frish and Webb<sup>3</sup> for direct optical measurements of vorticity. The technique, known as the Vorticity Optical Probe or VOP, is based on the propensity of spherical particles suspended in a flowing fluid to rotate with an angular velocity which is equal to one-half the local vorticity. Since the  $20 - 50 \mu\text{m}$  diameter spheres developed for this purpose are smaller than the smallest scale in liquid turbulent flows (the Kolmogorov microscale) and have small masses and moments of inertia, they have sufficiently rapid response times to react to the fastest fluctuations of vorticity and velocity in the flow.

To measure the angular velocity of such small particles, specially manufactured polymethylmethacrylate (PMMA or Plexiglas) spheres which contain one or more embedded lead carbonate crystals are used. The crystals are planar, highly reflective hexagons, typically  $16 \mu\text{m}$  wide and  $0.06 \mu\text{m}$  thick. When suspended in a liquid which matches the index of refraction of the PMMA, the spheres are invisible. A beam of light, such as from a laser, impinging on

such a sphere is reflected by the lead carbonate crystal in a direction determined by the relative orientation of the crystal surface with respect to the direction of the light beam's propagation. When the sphere rotates due to the presence of vorticity, the direction of the reflected beam changes with time. By placing an optical detector within the path of the reflected beam and measuring temporal changes in the direction towards which it is reflected, as indicated in Figure 1, the angular velocity of the sphere and thus the vorticity of the fluid is deduced.

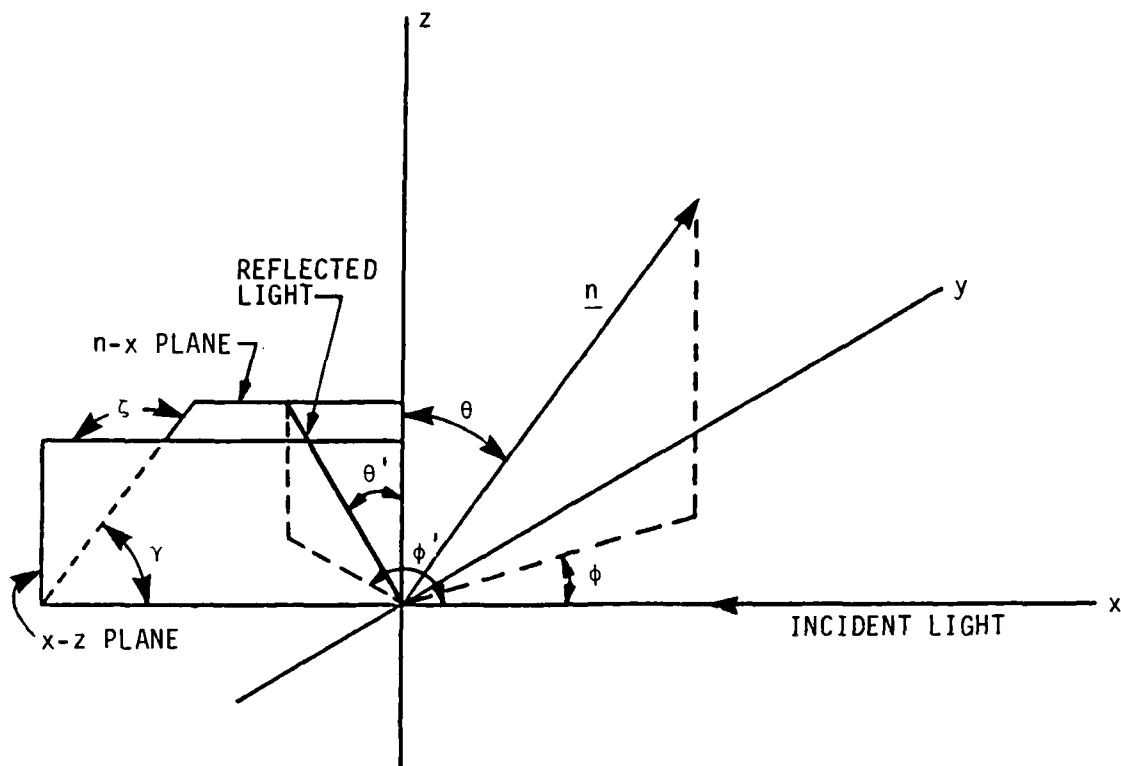
### 1.2.1 VOP Geometry

The coordinate system shown in Figure 2 illustrates the operation of the VOP. A light beam, incident along the x-axis, approaches the origin where a reflective particle is located. The mirror orientation, defined as the direction of its normal vector,  $\vec{n}$ , is given by the two angles  $\theta$  and  $\phi$ . The reflections emerge in the n-x plane at an angle defined in these coordinates as  $(\theta', \phi')$ . The vorticity of the particle  $(\omega_x, \omega_y, \omega_z)$  is determined by measuring  $\frac{d\theta'}{dt}$  and  $\frac{d\phi'}{dt}$ . To relate these measured values to  $\vec{\omega}$ , we first find the relationship between  $(\theta, \phi)$  and  $(\theta', \phi')$ .<sup>4</sup>



A-3402

Figure 1. Illustration of trajectory along a spherical surface of reflection from a mirror rotating with vorticity  $\omega$ .



A-3397

Figure 2. Coordinate system for analysis of reflection trajectory.

It is easiest to work entirely in cartesian coordinates. Thus

$$\hat{x} = \sin\theta\cos\phi \quad (1a)$$

$$\hat{y} = \sin\theta\sin\phi \quad (1b)$$

$$\hat{z} = \cos\theta. \quad (1c)$$

The x-axis and  $\vec{n}$  define a plane which forms an angle  $\zeta$  with the x-z plane and which contains both the incident and reflected beams. If  $\gamma$  is the angle between the x-axis and  $\vec{n}$  on this plane, then  $2\gamma$  is the direction of the reflection. Trigonometry yields



$$\hat{x} = \cos\gamma \quad (2a)$$

$$\hat{y} = \sin\gamma\sin\zeta \quad (2b)$$

$$\hat{z} = \sin\gamma\cos\zeta \quad (2c)$$

Equating Eqs. (1a-c) with (2a-c) yields

$$\cos\gamma = \sin\theta\cos\phi \quad (3a)$$

$$-\sin\gamma\sin\zeta = \sin\theta\sin\phi \quad (3b)$$

$$\sin\gamma\cos\zeta = \cos\theta, \quad (3c)$$

and solving for  $\theta$  and  $\phi$  in terms of  $\gamma$  and  $\zeta$  gives

$$\theta = \cos^{-1}(\sin\gamma\cos\zeta) \quad (4a)$$

$$\phi = \cos^{-1}(-\cos\gamma / \sqrt{1-\sin^2\gamma\cos^2\zeta}) \quad (4b)$$

Thence

$$\theta' = \cos^{-1}(\sin 2\gamma\cos\zeta) \quad (5a)$$

$$\phi' = \cos^{-1}(\cos 2\gamma / \sqrt{1-\sin^2\gamma\cos^2\zeta}) \quad (5b)$$

Solving now for  $\gamma$  and  $\zeta$  in terms of  $\theta$  and  $\phi$  and substituting back into Eqs. (5a and 5b) gives

$$\theta' = \cos^{-1}(\sin 2\theta\cos\phi) \quad (6a)$$

$$\phi' = \cos^{-1}[(\sin^2\theta\cos 2\phi - \cos^2\theta) / \sqrt{1-\sin^2\theta\cos^2\phi}] \quad (6b)$$

which are the desired relationships.

Now, if  $\theta$  and  $\phi$  vary with time, the rates of change of  $\theta'$  and  $\phi'$  are found to be

$$\begin{aligned} d\theta'/dt = [1/\sqrt{1-\cos^2\phi\sin^22\theta}] \\ \times [(\sin2\theta\sin\phi)d\phi/dt-(2\cos2\theta\cos\phi)d\theta/dt] \end{aligned} \quad (7a)$$

and

$$\begin{aligned} d\phi'/dt = [1/(1-\cos^2\phi\sin^22\theta)] \\ \times [(2\sin^2\theta-\sin^22\theta\cos^2\phi)d\phi/dt-(\sin2\theta\sin2\phi)d\theta/dt] \end{aligned} \quad (7b)$$

The rate of change of  $\vec{n}$  is related to the vorticity components by<sup>5</sup>

$$d\theta/dt = \omega_y \cos\phi - \omega_x \sin\phi \quad (8a)$$

$$d\phi/dt = \omega_z - \cot\theta(\omega_x \cos\phi + \omega_y \sin\phi) \quad (8b)$$

When an optical detector records the reflection passing through the orientation  $(\theta', \phi')$  relative to the incident beam, a unique relationship between the components of the vorticity vector and the local values of  $d\theta/dt$  and  $d\phi/dt$  (i.e., the local reflection trajectory) is established. Vorticity vector components can therefore be calculated by measuring  $d\theta'/dt$  and  $d\phi'/dt$  at that orientation. For example, at  $\theta = \pi/2$ , and  $\phi = \pi/4$ ;

$$\text{and} \quad d\theta/dt = (\omega_y - \omega_x)/2\sqrt{2} \quad (9a)$$

$$d\phi/dt = \omega_z/2, \quad (9b)$$

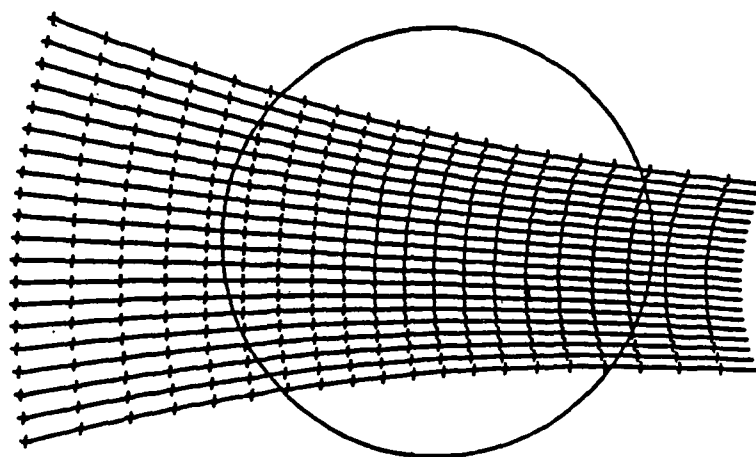
so that

$$\text{and} \quad d\theta'/dt = (\omega_y - \omega_x)/\sqrt{2}, \quad (10a)$$

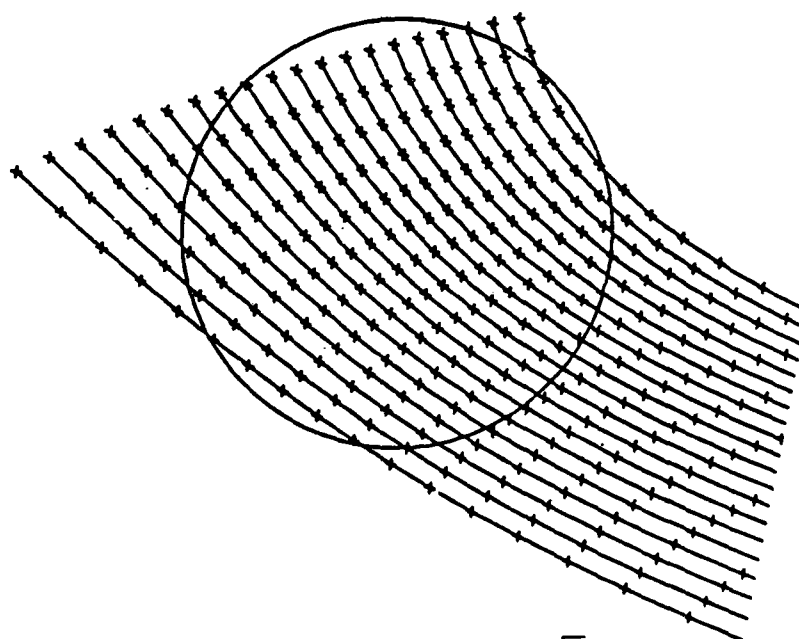
$$d\phi'/dt = 2\omega_z. \quad (10b)$$

### 1.2.2 Trajectory Simulations

In the general case of a large solid angle detector surface, Eqs. (7) and (8) do not reduce to the simple form of Eqs. (9) and (10) since  $\Theta(\vec{n})$  and  $\phi(\vec{n})$  can take on large ranges of values over which the reflections will strike the detector. The passage of the reflected beam across the detector surface is referred to as a reflection trajectory, or just trajectory. For any given vorticity vector, there is a corresponding family of trajectories, each member of which has a different initial mirror normal vector,  $\vec{n}$ , and thus traverses a different path on the detector. Figure 3(a-d) shows several simulated trajectory families for selected vorticity vectors. The trajectories traverse across a flat 1 sr solid angle surface. The angular coordinates of the surface (detector) center are  $\Theta = \frac{\pi}{2}$ ,  $\phi = \frac{\pi}{4}$  or  $\Theta' = \frac{\pi}{2}$ ,  $\phi' = \frac{\pi}{2}$ . Figure 3(a) shows possible trajectories for pure  $\omega_z$ , i.e.,  $\omega_x = \omega_y = 0$ . Figure 3(b) adds a component perpendicular to  $\omega_z$  and parallel to the "principal reflection plane", defined as that plane which would reflect the incident beam to the detector center. The effect of this additional vorticity component is mainly to incline the trajectories across the surface. Figure 3(c) includes yet another component, now perpendicular to this plane and thus also perpendicular to the two components of Figure 3(b). Note that the differences between Figures 3(b) and 3(c) appear almost entirely as subtle changes of trajectory curvatures. If this third component should become dominant as in Figure 3(d), reflections sweep about a coordinate singularity passing through the detector. Clearly, to analyze trajectories to yield all three components of vorticity using a single detector surface, it is essential to not simply record the rates at which reflections pass through the detector's center point, but to also determine precisely the local curvature of the trajectories.

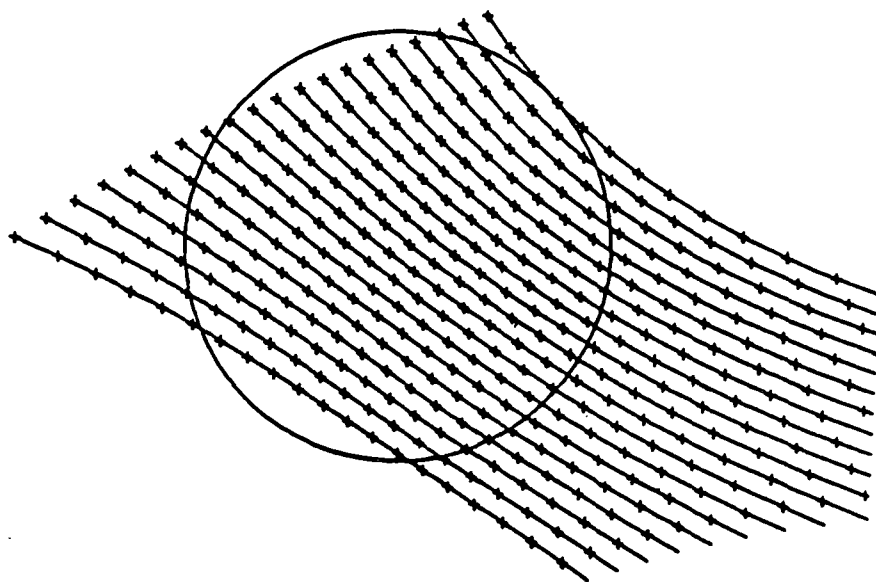


a)  $\omega_x, \omega_y = 0 \quad \omega_z \neq 0$

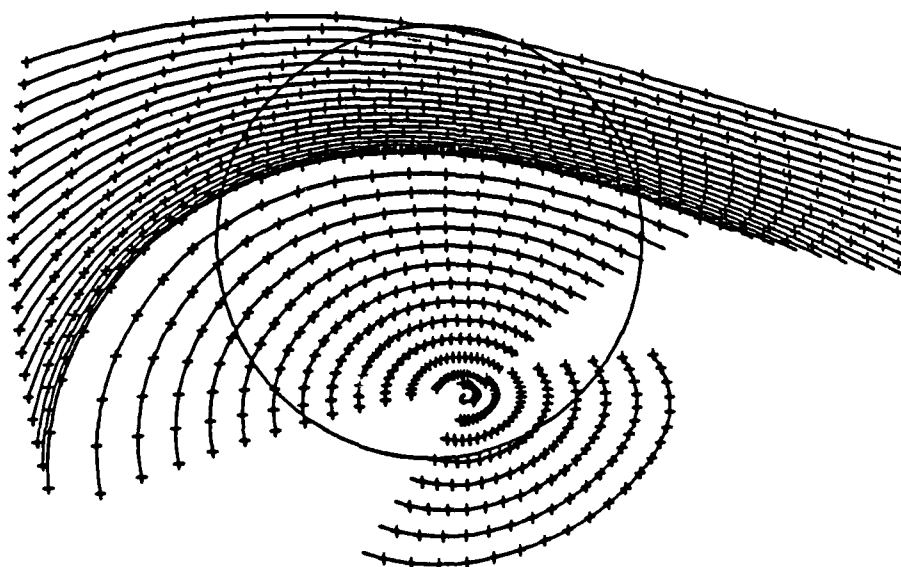


b)  $\omega_x + \omega_y = 0, \quad \omega_x - \omega_y = \sqrt{2} \omega_z$

Figure 3. Simulated reflection trajectory families over a flat 1 sr solid angle surface.



$$c) \quad \omega_x + \omega_y = \omega_x - \omega_y = \sqrt{2} \, \omega_z$$



$$d) \quad \omega_x = \omega_y = 2\sqrt{2} \, \omega_z$$

Figure 3. Continued.

### 1.3 PREVIOUS WORK

Prior to the current program, all work on the VOP was performed by the two authors of this report during their respective graduate careers at Cornell University. Originally, the VOP was tested using the optical system illustrated in Figure 4. To measure a single component of the vorticity vector over a small volume, which can be considered a single point, a laser beam enters the flow channel at a 45 degree angle through a prism used to prevent refraction of the beam. The flow channel is filled with a small concentration of randomly oriented VOP particles suspended in a liquid which matches the refractive index of the PMMA spheres. Usable vorticity measurements are generated by those particles which have mirrors oriented so as to reflect the laser beam at a nearly perpendicular angle within the plane defined by the

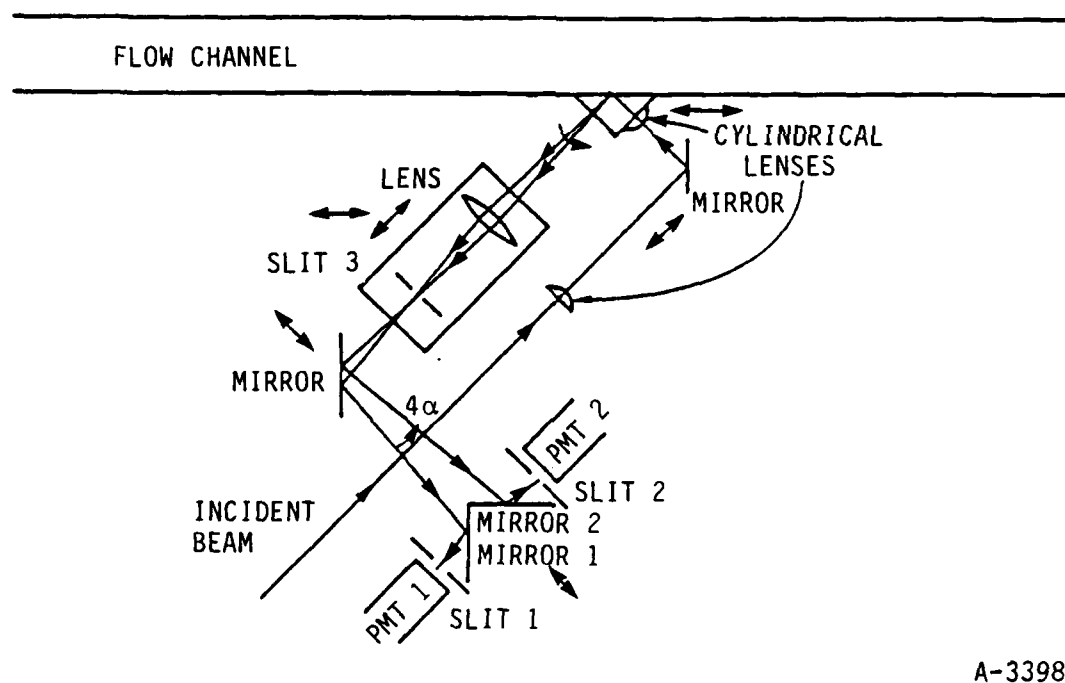


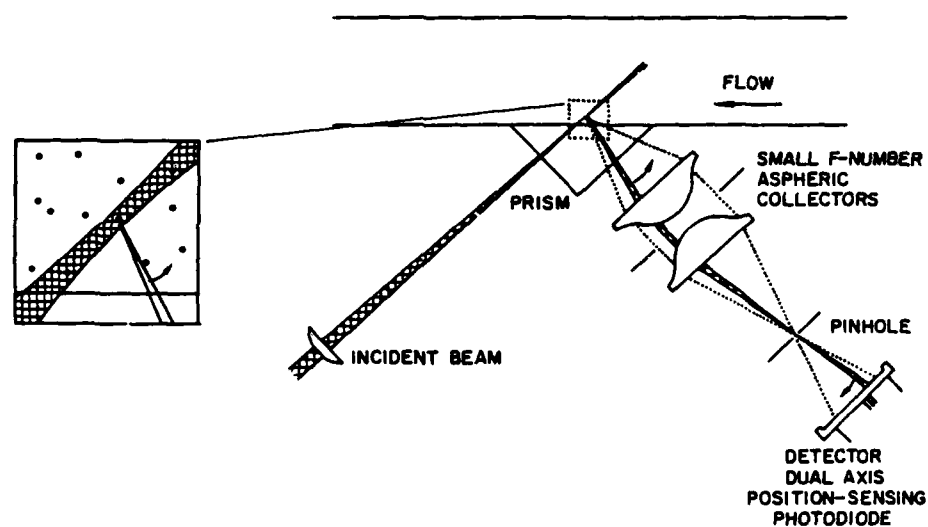
Figure 4. Original VOP optical detection system.

incident beam and the detecting optics. These particles are imaged onto slit 3 which, together with the incident beam, define the sampled volume. The rotational velocity of the reflected light from each properly oriented mirror is measured by observing its transit time across a small angle defined by a pair of closely spaced slits, shown as slits 1 and 2. Light passing through these slits is converted to electrical impulses by photomultiplier tubes (PMTs). The time between reception of sequential pulses from the two PMTs is a measure of the vorticity.

This system was tested in a laminar Poiseuille flow (see Appendix A) and used to measure spanwise ( $\omega_z$ ) vorticity fluctuations and profiles in a transitional boundary layer.<sup>4</sup> This system was restricted, however, to measurement of only the (dominant) spanwise component of vorticity ( $\omega_z$ ) in flows having large vorticity/velocity ratios. Also, the working fluid's refractive index was required to match PMMA (1.49). Organic liquids, specifically dibutylphthalate and p-cymene, were used for that purpose.

The second generation optical configuration,<sup>6</sup> shown in Figure 5, addressed the restriction on the vorticity/velocity ratio, but still required exotic fluids for index matching. The slits and photo-multipliers of the original system were replaced by a two-dimensional position-sensing photodiode enabling the simultaneous measurement of spanwise ( $\omega_z$ ) and streamwise ( $\omega_s$ ) vorticity components. The sampled volume was imaged onto the pinhole shown in the figure, and reflections traversed the photodiode. The photodiode produced analog signals corresponding to the (x,y) position of the reflection on the detector surface, providing not only a rate of passage, but the inclination of the trajectory. Near the detector center this information gives accurate estimates of two components of vorticity without requiring a minimum angular displacement, thus eliminating vorticity/velocity ratio restrictions. With an improved optical system, the second generation VOP could potentially yield all three vorticity components.

This second generation configuration was used to obtain simultaneous single-point measurements of  $\omega_z$  and  $\omega_s$  in a turbulent boundary layer. Considerable streamwise vorticity was observed. The limitations of this system were lack of water compatibility, and difficulty in discriminating between single (good) and multiple (bad) reflection events thus requiring elaborate off-line data analysis. Multi-point spatial vorticity correlations made with two such systems imaging adjacent points were confounded by temporally uncorrelated sampling, resulting in poor statistics.



A-8301

Figure 5. Second generation optical system for two-component vorticity measurement (from ref. 6).



## 2. PHASE I PROGRAM

As we had proposed, the Phase I program was divided into three distinct tasks. Task 1 demonstrated that all three components of the vorticity vector can be deduced from a single reflection trajectory across a single detector surface. Task 2 showed that many trajectories can be captured simultaneously, and be interpreted for data reduction. Task 3 was a demonstration of the feasibility of establishing the origins from which individual reflection emanate within the sampled volume. All of these tasks have been completed successfully, thereby demonstrating the possibility of assembling a system capable of volumetric vorticity measurement.

### 2.1 TASK 1 - THREE COMPONENT VORTICITY MEASUREMENT

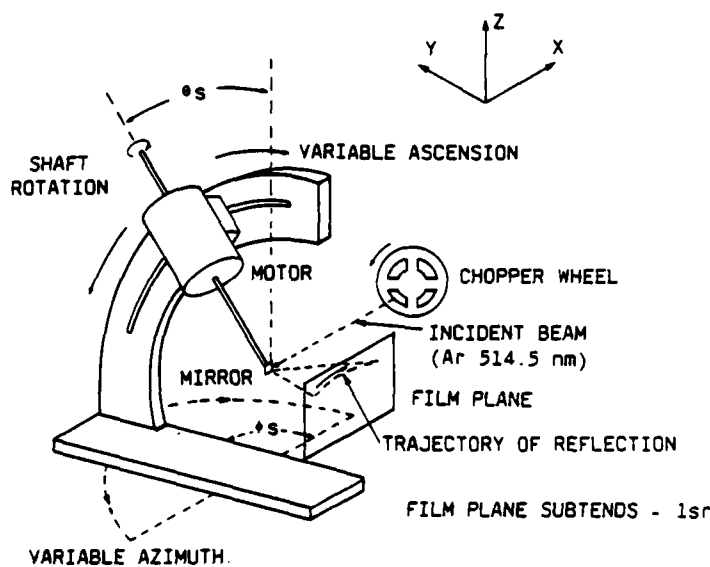
As discussed above, previous work on the VOP was restricted to measurements of one or two components of the vorticity vector, at one or two fixed positions in the flow. The simulated reflection trajectories of Figure 3 indicate, however, that careful analysis of the actual trajectories can yield all three vorticity components. In contrast to the concept of using two or more widely separated detectors as we had proposed for this measurement, the simulations showed that unambiguous vorticity values could be determined by making many measurements of  $d\theta'/dt$  and  $d\phi'/dt$  at modest angular separations along the surface of a single large-solid-angle detector. Therefore, for this task, a single photographic plate was used as the detector.

#### 2.1.1 Apparatus

Verification of three component vorticity measurement, its precision, and its sensitivity to various component mixtures and detection geometries, was most easily accomplished with a VOP simulation using a plane mirror, as in the apparatus shown in Figure 6a. The motor acted as an adjustable vorticity vector (magnitude and direction) and a plane mirror affixed to the shaft end served as the mock VOP mirror. A chopped Argon laser beam (514.4 nm) was incident

along the positive x-axis. Photographic film was used as detector. The film plane was parallel to the x-z plane, at any y value desired. The detection geometry was fixed in this way throughout Task 1.

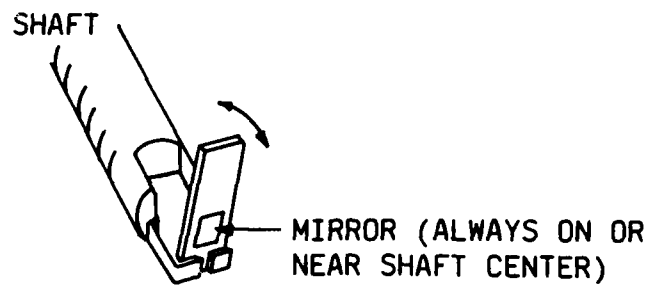
The chopped incident beam provided a time base so that, as the motor shaft turned, the reflections produced a sequence of spots or streaks on the film at known time intervals. The two-angle variable motor mount with variable speed motor allowed any mixture of the angular velocity components, and thus simulated vorticity components  $\omega_x$ ,  $\omega_y$ ,  $\omega_z$ , relative to the detection geometry while maintaining the mock VOP mirror precisely at the origin. Because the rotation axis can have any orientation relative to the incident beam, the orientation of mirror normal was made adjustable in order to insure that the reflections cross the film plane. Figure 6b shows details of the variable pitch mirror mount. The various orientations produce the individual members of trajectory families as described in Sub-section 1.2.2. Note that the measured vorticity must be independent of the orientation of the mirror normal.



A-8282

a) Task 1 apparatus for VOP simulation.

Figure 6. The rotating mirror.



A-8283

b) Adjustable pitch mirror mount.

Figure 6. Continued

The choice of photographic film as a detector was the logical one, since it provided a plane surface of large solid angle without imaging, and a convenient digitizable record for data analysis. The photographic film was 4 x 5 in. Kodax TMax 400 black and white, mounted in a double sided holder such that the film center corresponded to  $(0, Y_{\text{film}}, 0)$  in the geometry of Figure 6a. In all Task 1 experiments,  $Y_{\text{film}}$  was selected to be -10 cm so that the solid angle subtended by the film plane was  $\sim 1$  sr. The film was developed in our own darkroom, and reflection positions were electronically digitized using a digitizer pad coupled to an IBM-PC.

The entire apparatus of Figure 6a was placed in a light-tight enclosure. The film holder was mounted so that it could be remotely opened and closed. The laser entered the enclosure through a variable speed shutter. For each trial, the shutter speed was set to one motor rotation period. Thus the reflection crossed the film plane once and only once. With the essential VOP geometry abstracted in this way, this configuration provided a controlled test of our data analysis procedure and established the inherent precision of the method.

### 2.1.2 Data Analysis

Recorded reflection trajectories consisted of a sequence of  $N$  spots on the film. The film negatives were taped onto the digitizer pad, and the spot

centroids or edges were used for digitization. The position of the  $i^{\text{th}}$  spot in the sequence  $(X_i, Y_{\text{film}}, Z_i)$  was converted to reflection angular coordinates  $(\theta'_i, \phi'_i)$  during data reduction.  $\left(\frac{d\theta'}{dt}\right)_i$  and  $\left(\frac{d\phi'}{dt}\right)_i$  were computed from spot pairs:  $\left(\frac{d\theta'}{dt}\right)_i = \frac{\theta'_{i+1} - \theta'_{i-1}}{2\Delta t}$ ,  $\left(\frac{d\phi'}{dt}\right)_i = \frac{\phi'_{i+1} - \phi'_{i-1}}{2\Delta t}$ , where  $\Delta t$  is the chopped interval. Digitization errors produce uncertainties in the computed derivatives of  $\sim 1 \text{ s}^{-1}$ .

At least three equations are required to deduce a unique vorticity vector. The expressions (7a) and (7b) for  $\left(\frac{d\theta'}{dt}\right)_i$  and  $\left(\frac{d\phi'}{dt}\right)_i$  can be written

$$\left(\frac{d\theta'}{dt}\right)_i = a_i\omega_x + b_i\omega_y + c_i\omega_z \quad (11a)$$

$$\left(\frac{d\phi'}{dt}\right)_i = d_i\omega_x + e_i\omega_y + f_i\omega_z \quad (11b)$$

where the coefficients  $a$ - $f$  are functions of  $\theta'$  and  $\phi'$  which are determined entirely by the reflection geometry. Each trajectory produces  $2(N-2)$  such equations. To take full advantage of this information and produce the best  $\omega_{x,y,z}$  values which describe a trajectory, a linear least squares multiple parameter fitting algorithm was written. The data reduction program is included as Appendix B.

### 2.1.3 Measurements and Results

A series of photographs were made with several  $\vec{\omega}$  orientations and magnitudes. The test cases were:

1.  $\omega_x, \omega_y, \omega_z \neq 0$
2.  $\omega_x, \omega_y \neq 0; \omega_z \cong 0$
3.  $\omega_z \neq 0; \omega_x, \omega_y \cong 0$
4.  $\omega_z, \omega_x \cong 0; \omega_y \neq 0$
5.  $\omega_z, \omega_y \neq 0; \omega_x \cong 0$

These test cases demonstrate the capability to measure any vorticity vector orientation. They included the difficult example wherein  $\omega_x = -\omega_y$  and reflections sweep around a coordinate singularity passing through the film plane, as in Figure 3d. Of the data collected, two photographs, Figures 7 and 8, have been selected as representative of best and worst case precision.

Figure 7 is actually two trajectories on the same piece of film made sequentially with differing mirror pitches. This photograph is case 1;  $\omega_x, \omega_y, \omega_z \neq 0$ . For both pitches, the motor speed was 10 Hz, and the motor shaft orientation  $\theta_s = 20^\circ$ ,  $\phi_s = 140^\circ$ . For each pitch, the data reduction program generates the vorticity component values and their uncertainties, via the least square fit to the trajectory. These  $\omega$  values are then converted back into speed,  $\theta_s$ , and  $\phi_s$  for comparison. Table 1 compares the vorticity components calculated by this algorithm with the values expected from knowledge of the motor speed and orientation. Clearly the agreement is excellent.

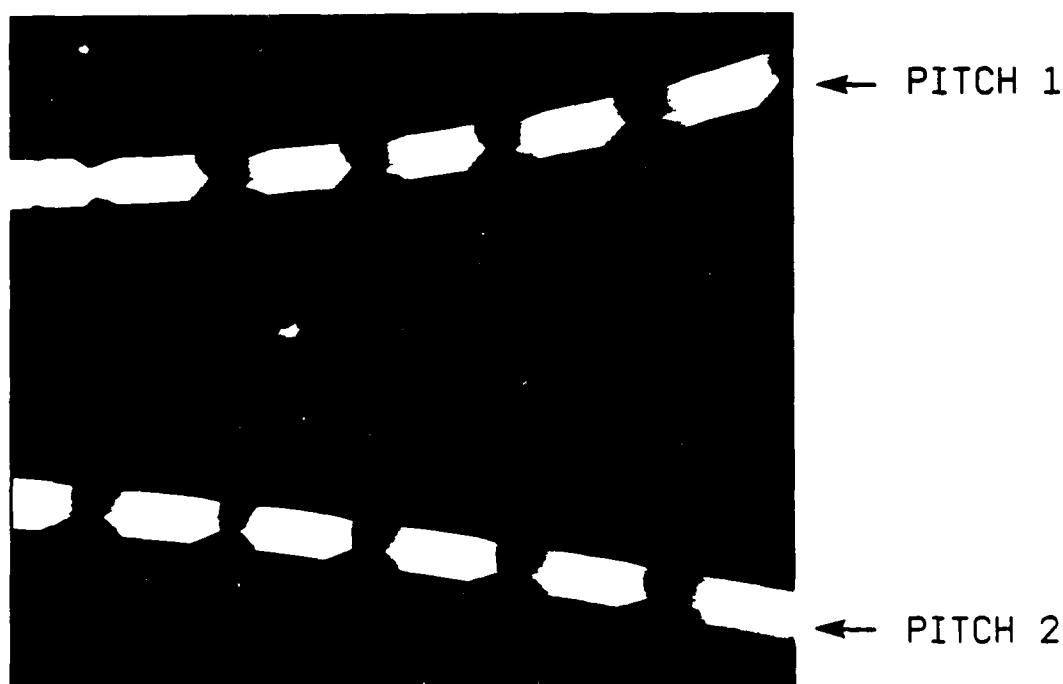


Figure 7. Photograph of two trajectories at different mirror pitches.  
 $\theta_s = 20^\circ$ ,  $\phi_s = 144^\circ$ .

TABLE 1.\*

Vorticity component calculated from trajectories in Figure 7.

	$\omega_z(s^{-1})$	$\omega_x(s^{-1})$	$\omega_y(s^{-1})$	Speed, $\theta_s$ , $\phi_s$
Pitch 1	-110.5 $\pm 2$	34.7 $\pm 4$	-29.1 $\pm 4$	9.05 Hz, 22.3°, 140°
Pitch 2	-123.6 $\pm 2$	34.6 $\pm 4$	-26.8 $\pm 4$	10.45 Hz, 19.5°, 142.2
Expected Values	-118.0 $\pm 6$	34.7 $\pm 4$	-25.3 $\pm 4$	10.00 Hz, 20.0°, 144°
*Chopping rate 600 Hz				

Figure 8 is case (2),  $\omega_z \approx 0$ ,  $\omega_x \approx -\omega_y$ . Extreme trajectory curvature is apparent. Again, two different mirror pitches are included in a single photo, but different motor speeds were used. The results are given in Table 2. Note the vorticity measurement in this case establishes the orientation of the motor shaft relative to the detection geometry ( $\theta_s$ ,  $\phi_s$ ) with greater precision than direct measurement, due to the large number of points and large trajectory angular size.

#### 2.1.4 Error Analysis

The results of Task 1 clearly demonstrate three component vorticity measurement capability under ideal conditions. The principal source of error in these measurements is digitization error. The precision with which the position of the centroid of each spot or streak on the film is established determines the fundamental precision of the vorticity measurement, which then scales with both the number of points and trajectory angular size. The curvature of the trajectory, which must be measured to determine the  $(\omega_x - \omega_y)/\sqrt{2}$  component, is most highly sensitive to this source of error.



Figure 8. Photograph of trajectories.  
 $\theta_S = 90^\circ$ ,  $\phi_S = 135^\circ$ .

TABLE 2\*.

Vorticity components calculated from trajectories in Figure 8.

	$\omega_z(s^{-1})$	$\omega_x(s^{-1})$	$\omega_y(s^{-1})$	Speed, $\theta_S$ , $\phi_S$
Pitch 1 (Outer)	$2.4 \pm 0.3$	$78.8 \pm 0.7$	$-77.7 \pm 0.4$	<sup>**</sup> 8.8 Hz, $88.8^\circ$ , $135.4^\circ$
Pitch 2 (Inner)	$3.1 \pm 0.3$	$129.6 \pm 0.6$	$-127.2 \pm 0.6$	14.5 Hz, $89.0^\circ$ , $135.5^\circ$
Expected Values	$1.0 \pm 0.0 \pm 2$	$88.9 \pm 6$	$-88.9 \pm 6$	10 Hz
	$2.0 \pm 0.0 \pm 2$	$133.3 \pm 8$	$-133.3 \pm 8$	15 Hz
*Chopping rate 600 Hz **Motor speed drifts from nominal values during trails. $\theta'_S$ , $\phi'_S$ independent of motor speed.				

The uncertainties of the vorticity components are typically:

$$\Delta\omega_z \leq 2\% \text{ of } |\vec{\omega}|, \text{ and}$$

$$\Delta\omega_x, \Delta\omega_y \sim 2\Delta\omega_z$$

The  $\chi^2_\nu$  goodness of fit statistics were generally  $\leq 1$ . This level of precision or better was observed in all five tests cases. Precision suffers with diminishing trajectory angular size, but could be improved with more accurate digitization methods. Misalignment of the incident beam or film plan introduced small additional systematic errors. Motor speed fluctuations also enter from photo to photo, but do not affect precise determination of  $\theta_s$  and  $\phi_s$ , which are independent of motor speed and serve as a basis of comparison. The dynamic range in  $|\vec{\omega}|$  is  $\sim 10$ . This is determined by the ratio of the maximum acceptable angular separation of "spots" to the minimum resolvable angle between them. This limitation is imposed by the use of photographic film and resolving spots by eye.

Having developed the analysis procedure and demonstrated the inherent precision of three-component vorticity measurement, we proceeded to study multiple simultaneous trajectories from actual VOP mirrors in Task 2.

## 2.2 TASK 2 - MULTIPLE TRAJECTORIES

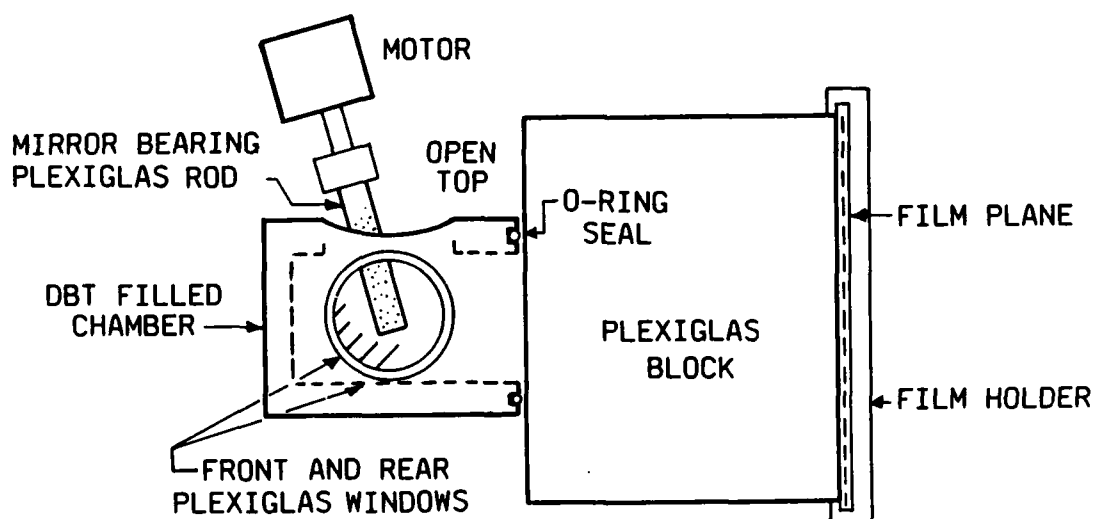
The remainder of the Phase I program was concerned with the development of volumetric vorticity measurement capability. In Task 2, we simultaneously recorded the trajectories of reflections from many lead carbonate (VOP) mirrors in a large volume. VOP mirrors embedded in a solid PMMA rod undergoing steady solid body rotation all have the same angular velocity vector. However, since the mirrors are randomly oriented, no two reflections will necessarily follow the same trajectory. Hence, this task provided a stringent test of the capability for three-component vorticity measurement at many points within the sampled volume.



### 2.2.1 Apparatus

A mirror bearing PMMA rod was manufactured by mixing a small quantity of Nacromer ZTX-B pearl pigment (containing lead carbonate mirrors), supplied by the Mearl Corporation, with the methylmethacrylate monomer. Bulk polymerization was carried out in test tubes using standard procedures.<sup>7</sup> Several rods with different mirror concentrations were produced. A concentration of  $\sim 10^3$  mirrors per  $\text{cm}^3$  was found to be most suitable for Task 2. The rod was machined to 7 mm diameter and mounted on the motor in place of the single mirror of Task 1.

As shown in Figure 9, to minimize both scattering at the rod surface and refractive deviation of reflections, the mirror-bearing rod was suspended in a refractive index-matching fluid chamber that was attached to a large Plexiglas block.



A-8300

Figure 9. Task 2 apparatus for multiple trajectory photographs.

The film holder was mounted as close as possible to the block face. The index matching fluid was dibutylphthalate (DBT). The front and rear Plexiglas chamber windows allow the passage of the incident beam. The laser power was  $\sim 0.5$  watts, and the beam diameter was 4 mm giving an illuminated volume of  $0.1 \text{ cm}^3$ . In all other respects, the apparatus and geometry were identical with that of Task 1.

### 2.2.2 Stationary Reflections

Figure 10 is a photograph of reflections from the stationary (i.e., non-rotating) rod. The exposure time was  $1/60$  sec. The characteristic appearance of the reflections' diffraction patterns results from the hexagonal shape of lead carbonate platelets.

The relatively poor contrast in the photo is due to the strong background scattering from the PMMA rod. This problem becomes even more severe with a

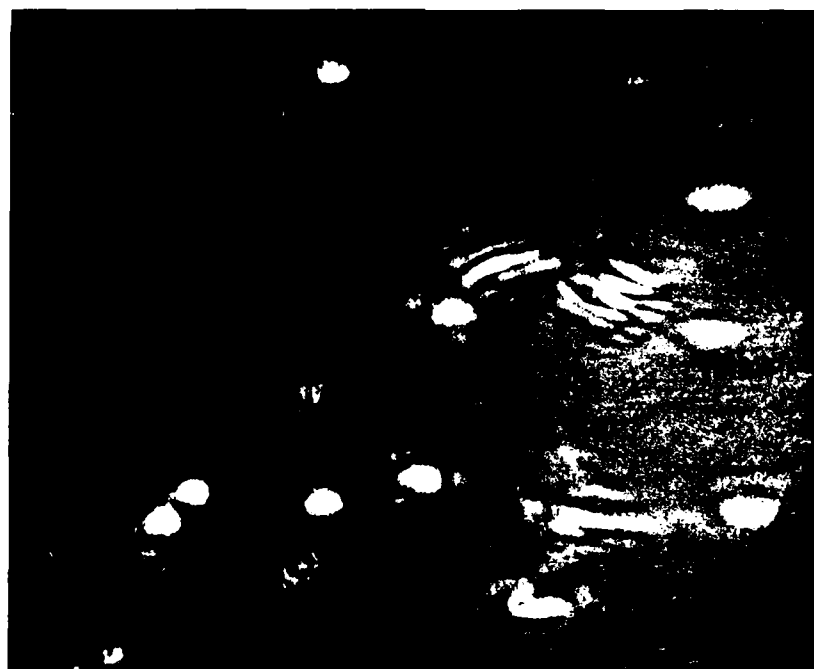


Figure 10. Photograph of reflections from lead carbonate mirrors embedded in the (stationary) PMMA rod.

rotating rod, where the short-lived reflections sweep past a nearly constant background, decreasing the signal to background ratio still further. An effective solution to this problem was to reduce the duty cycle of the chopper by covering 5/6 of the chopping wheel apertures. This reduced the number of reflection spots without affecting the brightness of those that remain while reducing the total background.

### 2.2.3 Task 2 Results - The Rotating Rod

The rod was set in motion at rotation rate of 8 Hz. The chopping rate was 800 Hz and several photographs were made. The photograph included here as Figure 11 is representative of the data obtained. Several valid trajectories, defined as those which have minimum of four points, were identified and labeled as A-M from film bottom to top. The unique shapes of the reflections

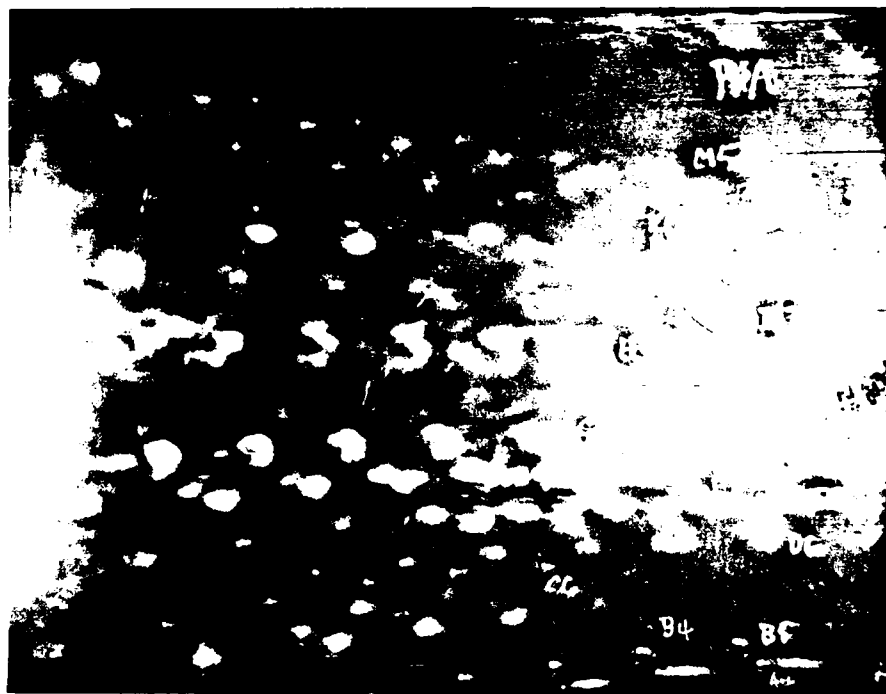


Figure 11. Trajectories of reflections from mirrors within the rotating PMMA rod, labeled (A-M). The bright dots are pencil marks used for digitization.

aid in trajectory identification by eye and generally a fixed feature was selected to aid digitization (centroid, edge, etc.). Vorticity values calculated from these trajectories are compared with expected results in Table 3.

TABLE 3.

Vorticity components calculated from photo trajectories A-M.

Trajectory (No. of Points)		$\omega_z$	$\omega_x$	$\omega_y$
Bottom of Film	A(5)	-101.4	22.9	-19.7
	B(5)	- 94.1	5.7	1.8
	C(6)	-104.3	37.0	-26.9
	D(6)	- 94.6	10.0	- 3.3
	E(8)	- 99.5	23.2	-20.0
	F(4)	- 99.5	38.6	-32.2
	G(5)	- 96.2	17.9	-15.0
	H(4)	-100.6	- 5.8	10.6
	I(7)	-103.1	19.7	-10.6
	J(6)	- 96.8	20.2	-11.7
	K(6)	- 95.4	18.3	-12.0
	L(8)	- 99.6	10.5	- 5.6
	M(5)	-100.3	16.8	-10.2
MEAN		- 98.9	18.1	-11.9
ST. DEV.		3.1	11.4	11.0

OR: 8.1 Hz,  $\theta_s = 12.4^\circ$ ,  $\phi_s = 146.7^\circ$

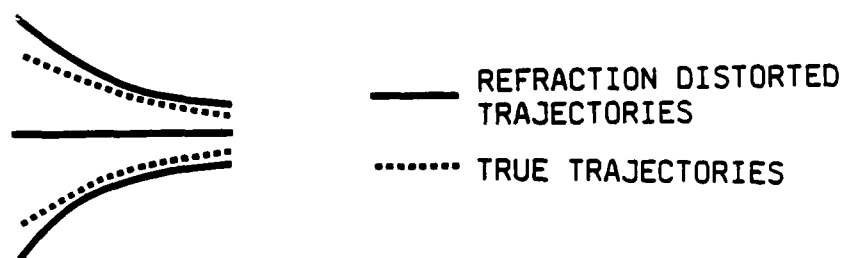
EXPECTED RESULT: 8.0 Hz,  $\theta_s = 12.0^\circ$ ,  $\phi_s = 140.0^\circ$

#### 2.2.4 Task 2 Discussion

Vorticity measurements for many VOP mirrors distributed throughout a finite volume have been obtained simultaneously in a single exposure. However, several features of this data need to be carefully examined. Since the number of points in each trajectory of Figure 11 are comparable to those of Figure 7 of Task 1, and the vorticity components are also comparable, we anticipate the standard deviations of the vorticity components in Table 3 should be similar to the uncertainties in vorticity components in Table 1. That is, the inherent precision of the vorticity measurement in Task 2 should be the same in Task 1. Apparently it is not. Goodness of fit statistics in Task 2 were in the range of  $1 \leq \chi^2_v \leq 20$ , indicating sources of error other than from digitization. The reason for this discrepancy is that there is more information in these data than has been accounted for in our analysis. As described below, some of this information is interpreted as measurement error, which could be eliminated by more sophisticated analysis.

These "errors" have three distinct sources. Digitization error has been discussed in Section 2.1.5 and is a fundamental limitation. The remaining effects are due to refraction, particle position, and particle velocity.

Refractive Effects. The film was not in intimate contact with the Plexiglas block as suggested by Figure 9. There was, in fact, a 4 mm air gap resulting in refraction at the air/plastic interface causing the effect indicated in Figure 12. Rays which passed through the center of the block (normal incidence) were projected onto the film plane correctly. However, rays which were incident on the Plexiglas surface at a non-normal angle were refracted to strike the film plane at an even larger non-normal angle. The greater the angle of incidence, the greater the spot displacement. This introduced curvature artifacts into the trajectories, which become more severe near the film perimeter. A straightforward correction for this effect was included in the data reduction program.



A-8281

Figure 12. Effects of refraction in air gap  
(greatly exaggerated in the figure).

In addition, due to a slight refractive index mismatch between DBT and our PMMA rod, there was additional refraction at the PMMA rod/DBT surface. Though the angular deviations from this source were very small, the relatively long path between the rod and the film resulted in spot displacements sufficiently large to affect trajectory shape. Also, because the interface is cylindrical and the origin of the reflections within unknown, this effect is essentially uncorrectable. It is, however, an artifact of this particular experiment and we emphasize that it would not exist under actual flow conditions with actual VOP particles.

Particle Position and Velocity Effects. The trajectory analysis used throughout this work assumes that all reflections emanate from the origin of the coordinate system in Figure 2. However, due to the non-zero diameter of the rotating rod, reflections actually originate offset from the origin and they translate as the rod rotates. These features result in apparent errors in vorticity determinations. Knowledge of the VOP mirror's position for each spot on the trajectory would re-establish the inherent precision of vorticity measurement seen in Task 1, with the additional benefit of providing the particle velocity. Conversely, it could be said that to obtain the vorticity measurement accuracy of Task 1, we must either measure the particle velocity or restrict the size of the measurement volume. However, all of the information needed to deduce the particle velocity can be encoded in the reflection trajectories; an independent measure of velocity is not required. Demonstrating this capability was the goal of Task 3.

### 2.3 TASK 3 - LOCATING REFLECTION ORIGINS (one-dimensional)

To study the shape and evolution of a coherent structure by measuring its characteristic vorticity field, the precise position and time from within a large volume at which a local vorticity vector is measured must be known. In addition, we learned in Task 2 that reflection origins must be known to achieve maximum precision in vorticity measurement. For these reasons, Task 3 was designed to demonstrate the feasibility of encoding reflection origin information in the reflected light itself.

#### 2.3.1 Task 3 approach

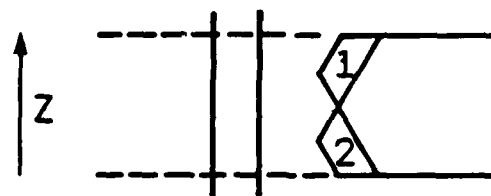
If the sampled volume is illuminated with two coincident beams of different color, the reflections will of course contain the two colors as well. Then, if known spatial intensity gradients are imposed on one or both of the colors along the z-direction for example as in Figure 13, it is possible to determine the Z coordinate by observing the ratio of reflected intensity of the two colors.

For intensity gradients in color 1 and color 2 respectively of:

$$I_1 = f(z) \text{ (e.g. } az + b), I_2 = g(z), \quad (12)$$

the ratio of reflected intensity at position Z is:

$$I_1/I_2 = f(z)/g(z) \equiv h(z), \quad (13)$$



A-8299

Figure 13. Coincident beams of different color or polarization.

where  $h(z)$  is a well-determined monotonic function of  $Z$ . The measured  $I_1/I_2$  ratio corresponds to a unique  $Z$  value. This procedure can, in principle, be extended to multiple dimensions but, as discussed later, other methods in conjunction with the one-dimensional measurement may eliminate the need for more than two colors.

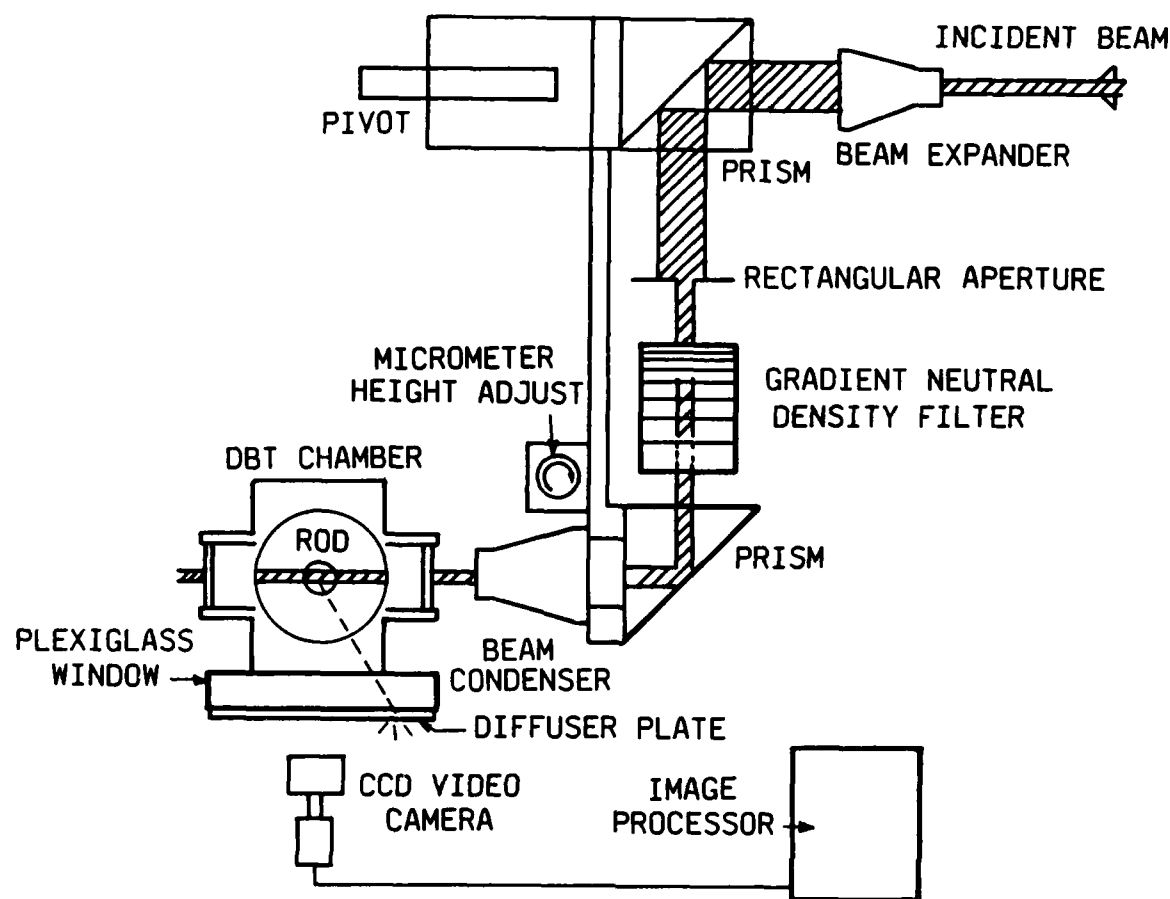
We had proposed to perform this measurement by separating the 5145Å and 4480Å lines emitted by our Argon-Ion laser, imposing an intensity gradient on one color, and then recombining the two beams prior to illuminating the PMMA rod. The reflections were to be captured on color photographic film, which would have been analyzed by microdensitometry to yield the color intensity ratios. Unfortunately we had not realized at the time that these two colors are not sufficiently distant from one another in wavelength to be easily discriminated in color photographic film. Since no other color or laser was immediately available, we chose an alternate approach which demonstrated the validity of the method, albeit in a somewhat less colorful manner, when used in conjunction with modern electro-optic detectors and processors.

### 2.3.2 Apparatus

The simple demonstration of this measurement employed a single color of light and two successive stationary reflections, illuminated by beams having two different imposed intensity gradients. A digital video system was used to capture and compare images of the reflections. Figure 14 shows the Task 3 optical configuration.

The incident beam was colinear with a pivot about which the optical apparatus (but not the rod or the chamber) turns. This allowed adjustment (via the micrometer screw) of beam position along the rod's axis without altering the optical path. The beam was expanded and passed through a rectangular aperture, thereby providing a nearly uniform intensity "top-hat" beam with sharp edges. The top-hat beam passed through a Newport Corporation linear gradient neutral density filter, which imposed a roughly linear intensity





A-8296

Figure 14. Task 3 optical configuration for intensity gradient position measurement.

gradient from top to bottom (the z-axis, normal to page in the figure). This gradient filter could be inverted to provide an intensity gradient in the opposite sense. The beam was then condensed to desired cross-section and directed through the DBT chamber to the mirror-bearing rod. The reflections on the Plexiglas diffuser plate were then viewed with a Sierra Scientific CCD camera equipped with a 50 mm lens. The camera output was coupled to a Data Translation Model DT2851, Frame Grabber and Compaq 286 computer, which enabled capture and digitization of individual camera frames. Each frame comprised 512 x 512 individual pixels digitized to 8-bit accuracy. The amplitude of the digitized signal at each pixel is linearly proportional to the energy incident on that pixel during the exposure time, plus a fixed offset.

### 2.3.3 Experimental Procedure

Direct Position Measurements. In order to test the intensity gradient technique, the Z positions of individual mirrors first were measured directly and then compared to the positions predicted by the gradient method. The direct measurements were accomplished by using the micrometer screw to raise and lower the rectangular beam along the mirror bearing rod's axis (i.e., the z-axis). From a standard starting position, the beam was lowered until a particular reflection vanished from the diffuser plate, then raised from this position until it vanished once more. This gave the beam height. The beam was then lowered to the standard position leaving the particle at a known Z position within the incident beam. In this way many individual reflections were measured and catalogued as the motor shaft was turned by hand.

Intensity Gradient Measurements. To compare the direct position measurements with the intensity gradient measurement, two images were captured for each reflection or group of reflections within the CCD camera field of view. The first image had the approximately linear intensity gradient oriented so that the brightest part of the incident beam was near the top. This is abbreviated as the gradient "up" image. The gradient filter was then inverted to capture the second gradient "down" image.

To analyze these images, subtraction of the fixed background is required, as is a calibration of the intensity gradient. To measure the background signal, the rod was rotated to a position where no reflections could be seen in the field of view and only the bright background was visible. This scene was recorded gradient "up" and "down". The calibration was accomplished by a similar method. The DBT chamber and rod were removed, and the incident beam was projected directly onto the diffuser screen. Images of it were also recorded gradient "up" and "down".

Image analysis. A video processing routine was written to perform background subtraction and divide "up" frames by "down" frames. The resulting ratios

were found to be quite uniform over an individual reflection's image. Figure 15 shows such a processed image. The frame division has been performed only over the rectangular area on the spot (at upper left) since the signal/noise ratio degrades near the reflection's edge. An intensity profile across the reflection (along the line visible in the photo) is also shown. The values are one-hundred times the actual intensity ratio.

Similar processing of the calibration image provided a measure of intensity ratios at every position in the incident beam. The calibration and its corresponding profile are shown in Figure 16. To establish the z-coordinate of a particular reflection origin, it remains only to find the position along the calibration curve of Figure 16 where the intensity ratio is the same as that observed in the reflection.

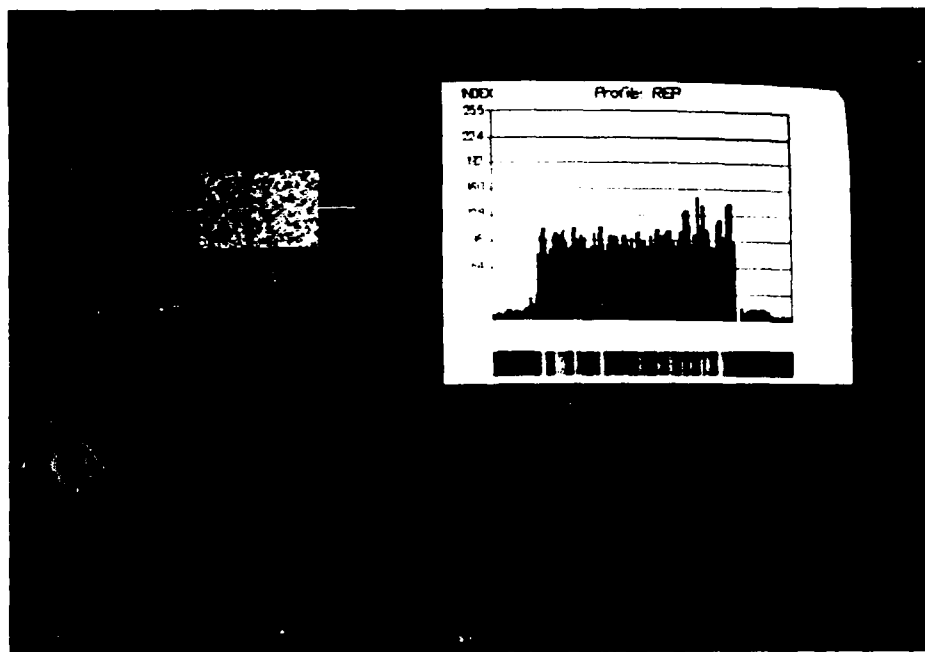


Figure 15. False color enhanced video display of gradient "up" frame (background subtracted) after division by the corresponding "down" frame within the rectangular area on the reflection at upper left.

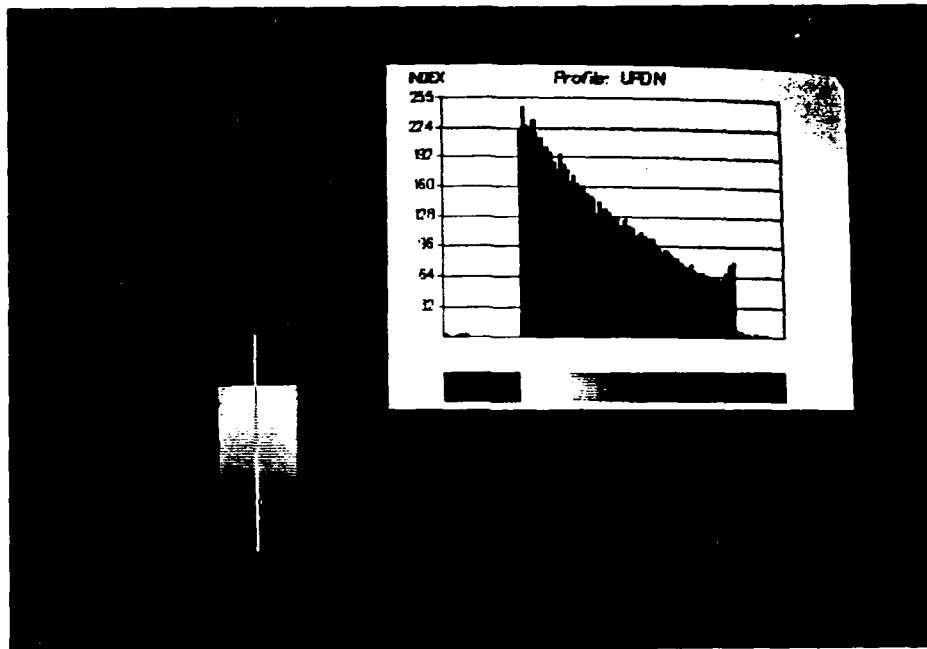
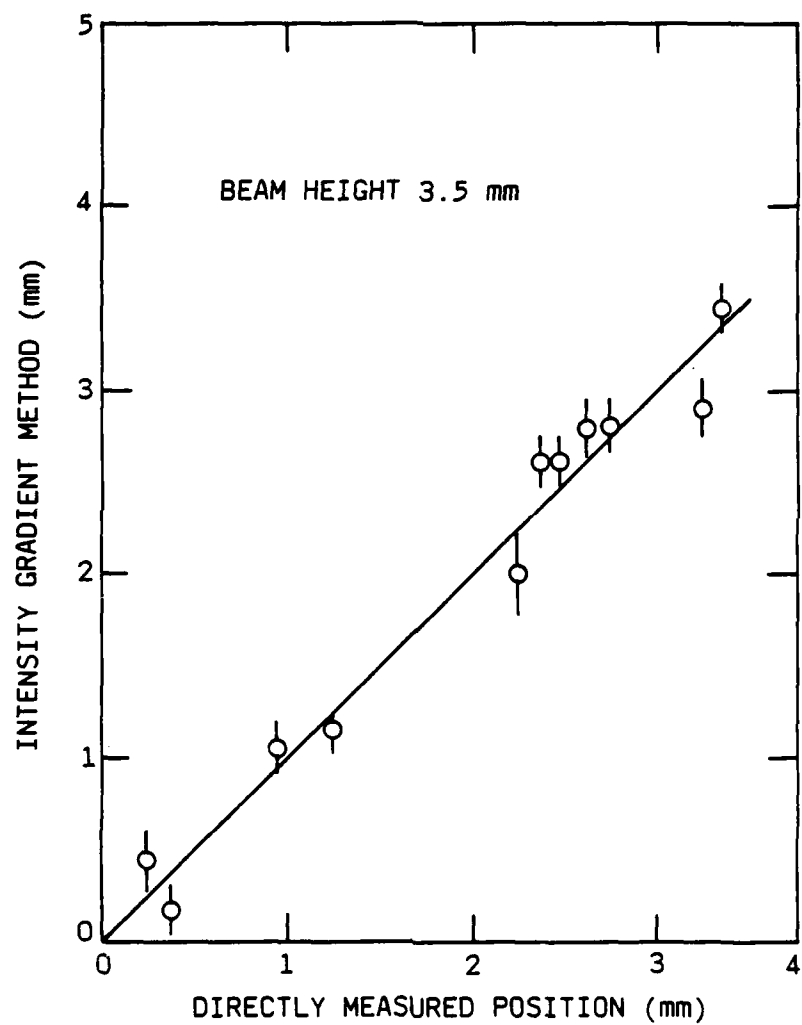


Figure 16. Calibration band. Division has been performed over the directly imaged incident beam cross-section.

#### 2.3.4 Task 3 Results

Figure 17 is a plot of the direct measurements against the intensity gradient measurements. The calibration curve was also employed to convert uncertainty in reflection ratios to uncertainty in particle positions. Position errors result from small variations in gradient uniformity or differences in the optical path between successive images. The intensity gradient method gives ~200  $\mu\text{m}$  precision over the 3.5 mm beam. This is less than 10 VOP particle diameters.



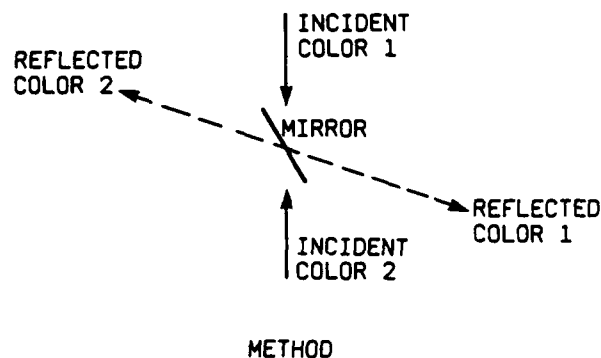
A-8295

Figure 17. Comparison of intensity gradient method and direct measurement of z-position.

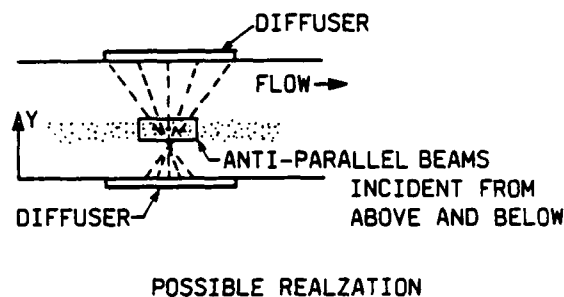
## 2.4 CONCLUSIONS

In this program, experiments were performed that demonstrated the feasibility of expanding the extant vorticity optical probe technology to include three component vorticity measurement and volumetric applications. Precise three component vorticity measurement has been demonstrated at a single point and at many points within a volume. However, it has been found that the best accuracy is achieved when the location of the reflection origin is well known for each point (spot) on the trajectory. A possible method for determining these locations has been demonstrated, using state-of-the-art digital video technology.

Knowledge of particle positions along a reflection trajectory (i.e. as a function of time) is, of course, equivalent to particle velocity measurement. Though the feasibility of measuring one position coordinate has been demonstrated, its extension to more than one dimension may not be straightforward. The difficulty is in obtaining multiple colors of sufficient intensity to enable detection of reflections rotating at speeds as much as 100 times those used in this Phase I program. It is conceivable that this information can be obtained from the reflection trajectories by performing a more complete mathematical analysis. Specifically, the analysis of Section 1.2.1 could be modified to include the six additional unknowns  $X_0$ ,  $Y_0$ ,  $Z_0$ ,  $U$ ,  $V$ ,  $W$ . However, preliminary examination of the full (nine unknowns with  $\vec{\omega}$ ) description of trajectories indicates that many of these variables may be too strongly coupled to be determined from a single trajectory. Furthermore, they do not enter in the simple linear fashion that so greatly simplified the vorticity analysis. It would be preferable to design experiments which provide the auxiliary data to make such an analysis possible. A potential approach, shown in Figure 18, employs coincidence detection on two opposed detectors. Oppositely directed beams produce spot pairs on the detectors; the reflection origin must lie on the line joining these spots. An independent depth determination (along  $y$  in the figure) using a version of the intensity gradient method, for example, would give complete position and velocity information.



A-8284



A-8285

Figure 18. Coincidence method for complete vorticity and velocity determination.

Also the similarity of the patterns on the detectors (with simple corrections for the mean velocity) would facilitate automated trajectory identification and data reduction.

For non-volumetric applications, the VOP with three component capability is itself a valuable instrument which may have commercial appeal. The principal obstacle to its wide-spread applicability remains the lack of water compatibility. We have studied this problem and believe that there are several possible solutions. The most appealing is to manufacture VOP particle from one of a variety of low refractive-index fluorinated oils or plastics. Upon solving this problem, we believe that a prototype (single point) VOP is quickly realizable.

We hope to have the opportunity to address and overcome these issues in a Phase II program. The first objective of Phase II would be to manufacture VOP particles which can be used in common laboratory water flow tunnels. Upon achieving this goal, we would proceed with development of a prototype commercial system able to measure the vorticity vector at a single point in the flow. A small water flow system would be assembled for use in testing the

prototype. Concurrently, we would continue the development of a volumetric measurement capability, addressing the details of three-coordinate position measurement and of tracking multiple trajectories from rapidly rotating mirror-bearing spheres.



### References

1. Freymuth, P., "Visualizing the Combined System of Wing Tip and Starting Vortices," in Flow Lines, TSI Inc., St. Paul, MN (May 1986).
2. Blackwelder, R.F. and Kaplan, R.E. "On the wall structure of the turbulent boundary layer." J. Fluid Mech. 76, 89 (1976).
3. Frish, M.B. and Webb, W.W., "Direct Measurement of Vorticity by Optical Probe," J. Fluid Mech., 107, 173 (1981).
4. Frish, M.B., "Direct Measurements of Vorticity in a Nearly Turbulent Boundary Layer," Ph.D. Thesis, Cornell University (1981).
5. Johnson, D.H., "Measurement of the Rate of Strain Tensor in a Turbulent Flow Using Light Scattering from Axisymmetric Particles," Ph.D. Thesis, Cornell University (1975).
6. Ferguson, R.D. and Webb, W.W., "The Vorticity Optical Probe: A Fast Multicomponent Model," Proc. of 8th Biennial Symp. on Turbulence, University of Missouri-Rolla (1983).
7. Rodriquez, F., Principles of Polymer Systems, McGraw-Hill (1970).

APPENDIX A

## Direct measurement of vorticity by optical probe

By MICHAEL B. FRISH AND WATT W. WEBB

School of Applied and Engineering Physics, Cornell University, Ithaca, N.Y. 14853

(Received 12 April 1980)

An optical method for the direct measurement of vorticity in liquid flows is described. At the present state of development it is capable of responding to vorticity fluctuations with a response time of about 1 msec and a spatial resolution of better than  $50\text{ }\mu\text{m}$ . Small spherical particles suspended in the flow rotate with angular velocity accurately equal to half the local vorticity; thus measurements of the rotation rates of such particles indicate the vorticity. Transparent spherical particles of less than  $50\text{ }\mu\text{m}$  diameter, each containing embedded planar crystal mirrors, have been developed for this purpose and are suspended in a refractive-index-matched liquid. Measurements of the times required for laser reflections from the mirrors to rotate through the small angle defined by a pair of slits yields the rotation rate, and thus the vorticity. Production and physical properties of the probe particles are reported. Theoretical capabilities and limitations of the method, including accuracy, spatial and temporal resolution, data rate, and background noise are calculated and found to be coupled to the optical geometry and flow field. Analysis yields procedures for selective optimization of each parameter as dictated by the particular application. Measurements of steady-state, laminar, two-dimensional Poiseuille flows demonstrate the effectiveness of the technique and confirm theoretical predictions.

### 1. Introduction

Although the vorticity field,  $\omega(\mathbf{x}, t) = \nabla \times \mathbf{v}(\mathbf{x}, t)$ , is an essential property of rotational and turbulent flow, requisite measurements of the vorticity transcend experimental capability. Modern techniques of hot-wire and hot-film anemometry and laser-Doppler anemometry can measure components of the velocity field  $\mathbf{v}(\mathbf{x}, t)$  at a limited number of points. The velocity components are ordinarily analysed by finite differences or application of Taylor's frozen-flow hypothesis to calculate the vorticity (see, for example, Eckelmann *et al.* 1977; Foss 1977; Willmarth & Bogar 1977), but error magnification by the necessary differentiations limits the accuracy and spectral range. Spatial resolution of the method has usually been limited to about 0.1 cm by hot-wire probe geometry although Willmarth & Bogar (1977) have recently reported a spatial resolution of  $100\text{ }\mu\text{m}$ . In principle flow perturbations can be avoided and the spatial resolution can be slightly improved by laser-Doppler anemometry but the complexity of these simultaneous optical measurements has apparently deterred its application to vorticity measurement.

The ideal system for vorticity measurement should meet these criteria: Spatial resolution exceeding the inner scale of turbulence  $\eta$  ( $\eta \sim 50\text{ }\mu\text{m}$  in common liquid flows), temporal resolution exceeding the shortest expected vorticity fluctuation time,

and data acquisition rates, spectral range and measurement accuracy sufficient for calculation of vorticity correlation functions and higher moments of vorticity.

The potential of such measurements of vorticity has motivated a disparate approach to this difficult measurement problem. Encouraged by the successful development of a method of optical scattering from anisotropic, submicroscopic particles for direct measurement of the strain-rate tensor with excellent spatial resolution (Johnson & Webb 1972), a new optical method for direct measurement of vorticity distributions in liquids with  $50\text{ }\mu\text{m}$  spatial resolution has been developed and is described here. It is based on the propensity of small spherical particles suspended in flowing fluid to accurately track the local vorticity  $\omega$  by rotation with angular velocity  $\Omega = \frac{1}{2}\omega$ . Reflections from a dispersion of small transparent plastic spheres each containing one or more flat, highly reflecting mirrors provide the desired indicator of local vorticity. To measure vorticity, a few volume per cent of these particles are added to a transparent liquid of matching refractive index. A laser beam illuminating a small volume of the flow to be sampled is reflected by the rotating particles. The rotational velocity of each reflected beam, which equals the local vorticity at the reflecting particle, is measured by observing the transit time of the reflected beam across a small angle defined by a pair of closely spaced slits. Each such transit provides a datum for prompt on-line calculation of the instantaneous local vorticity that is stored for analysis of the vorticity distribution. This measurement system is here called the vorticity optical probe or VOP for brevity.

The vorticity measurement system is described in §2 of this paper. There the processes of manufacture and the physical properties of the probe particles are reported in some detail. This is followed by a description of the data collection system designed for application to laboratory scale wakes, mixing layers and boundary layers in channels at modest Reynolds numbers. The characteristics of the detected reflexions, which tend to limit the precision of the technique, depend on both reflecting particle properties and optical-system geometry. The optical geometry its and effect on measurement performance are discussed and the signal acquisition and data-processing procedure are described.

Section 3 presents a theoretical discussion of basic experimental capabilities and limitations of the method including accuracy, spatial and temporal resolution, data rate and background noise, and their dependence on experimental parameters. To describe how the interplay of inhomogeneity of flow with the optical geometry and the optical imperfections limits the available vorticity measurement resolution a system-resolution function is defined.

Section 4 describes experimental tests of the measurement system by application to steady-state Poiseuille flows. Measured vorticity distributions confirm theoretical expectations and demonstrate the effectiveness of the vorticity optical probe.

Finally in §5 the properties of the vorticity optical probe system are summarized and prospects for applications and future development are discussed.

## 2. Vorticity measurement system

### 2.1. Fundamental concepts

The vorticity measurement system comprises: (1) the spherical probe particles containing planar mirrors; (2) refractive-index-matched fluid; (3) optical system; (4) data acquisition and analysis system.

Each aspect of the system will be discussed in turn. First, however, the fundamental hypothesis that small spherical particles follow the flow must be established.

Chwang & Wu (1974) have calculated the couple due to local vorticity acting on small particles of various shapes with results that agree with the early calculation of Jeffrey (1922) for spheroids. Application of their results shows that the spherical probe particles faithfully follow flow fluctuations that occur on a time scale slower than about 1 ms. The calculations are valid when the Reynolds number based on particle radius  $r$  and velocity  $u$  relative to the surrounding fluid is much less than unity. Stokes' law suggests that relative velocity will relax exponentially with relaxation time

$$\tau_u = \frac{2}{3} r^2 \rho / \mu, \quad (2.1)$$

where  $r$  is the sphere radius,  $\rho$  the particle density, and  $\mu$  the dynamic viscosity. With appropriate data for the probe particles,  $\rho = 1.2 \text{ g cm}^{-3}$ ,  $\mu = 0.005 \text{ g cm}^{-1} \text{ s}^{-1}$  and  $r = 25 \times 10^{-4} \text{ cm}$ , the relative velocity relaxation time is  $\tau_u \sim 0.4 \text{ ms}$ . Hence, the calculation of Chwang & Wu is valid for the probe particles for time scales  $\gtrsim 1 \text{ ms}$ .

Chwang & Wu's equation (11) gives the torque on a sphere of radius  $r$  rotating at angular velocity  $\Omega$  relative to the surrounding fluid as  $M = -8\pi\mu r^3\Omega$ . Thus the relative rotational relaxation time is

$$\tau_r = \frac{1}{15} r^2 \rho / \mu. \quad (2.2)$$

For the probe particles  $\tau_r \sim 0.1 \text{ ms}$ .

The shortest time scale in turbulent flow is the Kolmogorov micro-scale of time (Tennekes & Lumley 1972)

$$\tau_k \sim (l/u) R_l^{-1/2}, \quad (2.3)$$

where  $R_l$  is the turbulence Reynolds number,  $l$  the integral length scale, and  $u$  the turbulent velocity. Extreme values in laboratory water tunnel flows are  $l \sim 0.3 \text{ cm}$ ,  $u \sim 7 \text{ cm s}^{-1}$ , and  $R_l \sim 200$  (Frenkiel, Klebanoff & Huang 1979), giving  $\tau_k = 3 \text{ ms}$ . Therefore the probe particles should readily follow rotational and translational fluctuations in anticipated turbulent liquid flows.

This line of analysis also provides, following Jeffrey (1922), an estimate of the possible measurement error due to non-spherical particles that might be formed by damage or adhesion of spherical probe particles. Non-spherical particles do not rotate with the same angular velocity as the fluid. Their long axes tends to align with the principal strain rate in a non-uniform flow. Approximating an adherent pair of spheres by an ellipsoid of major axis  $4r$  yields a variable rotation rate of the form

$$\Omega_p = \frac{4}{5} \frac{1}{1 + 3 \sin^2 [\frac{2}{3}(dv/dy)t]}, \quad (2.4)$$

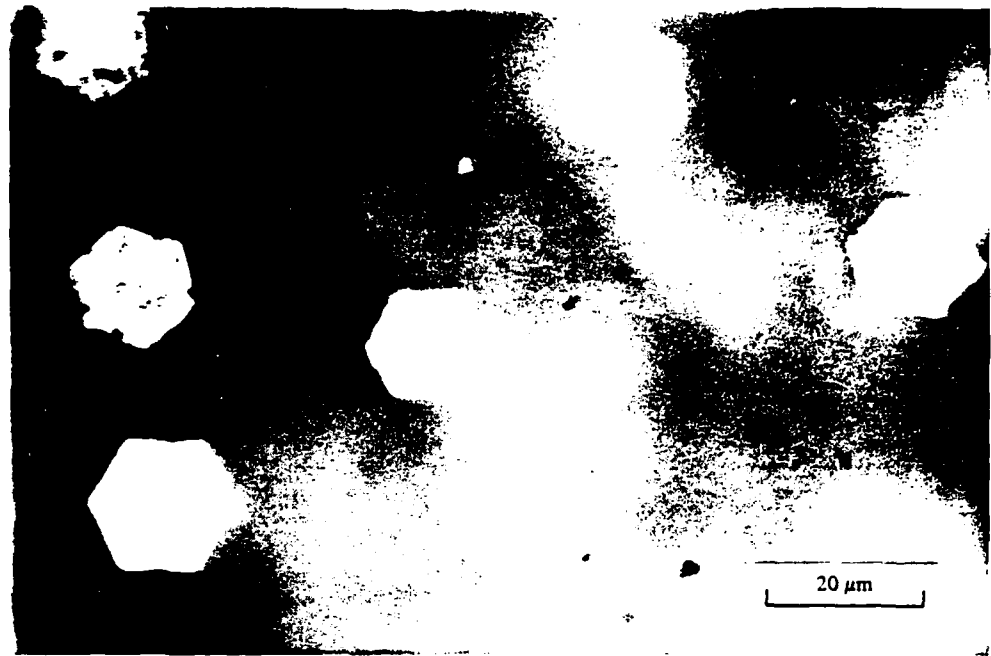


FIGURE 1. Photomicrograph of basic lead carbonate crystals in reflected light.

where  $dv/dy$  is the maximum magnitude of the local velocity gradient. The rotation rate  $\Omega_p$  of this ellipsoid varies from the rate  $\Omega$  for spherical particles within the limited range

$$\frac{2}{3}\Omega < \Omega_p < \frac{5}{3}\Omega. \quad (2.5)$$

Thus defective probe particles would contribute a broadened background to vorticity measurements.

Rotation of the probe spheres should not be perturbed by inter-particle interaction and they should not perturb the fluid flow. Jeffrey (1922) showed that the effective viscosity of the bulk fluid will be increased by a factor of  $1 + 2.5V$  by the addition of a volume fraction  $V$  of solid spherical particles. Thus the probe particle number density  $n$  should be limited so that the volume fraction of particles is small, that is  $\frac{4}{3}\pi r^3 n \ll 1$ . For spheres of  $25\mu\text{m}$  radius this requires  $n \ll 1.5 \times 10^7 \text{ cm}^{-3}$ . A more-than-ample concentration,  $10^6$  particles  $\text{cm}^{-3}$ , increases the viscosity by only 10 %.

## 2.2. Probe particles

The preceding section indicates that spherical particles of radius  $r \lesssim 25\mu\text{m}$  and moderate density accurately sample the local vorticity. They rotate at an angular velocity  $\Omega$  equal to half the local vorticity  $\omega$  (Batchelor 1967, §§ 2.3, 2.4). Uniform dispersion of the particles requires that they not stick together and that the particle density approximate that of the fluid. To minimize light scattering the refractive index of the particles must closely match that of the fluid. The essential development enabling this optical method for vorticity measurement is the process for production of large quantities of transparent spherical particles containing planar mirrors. The

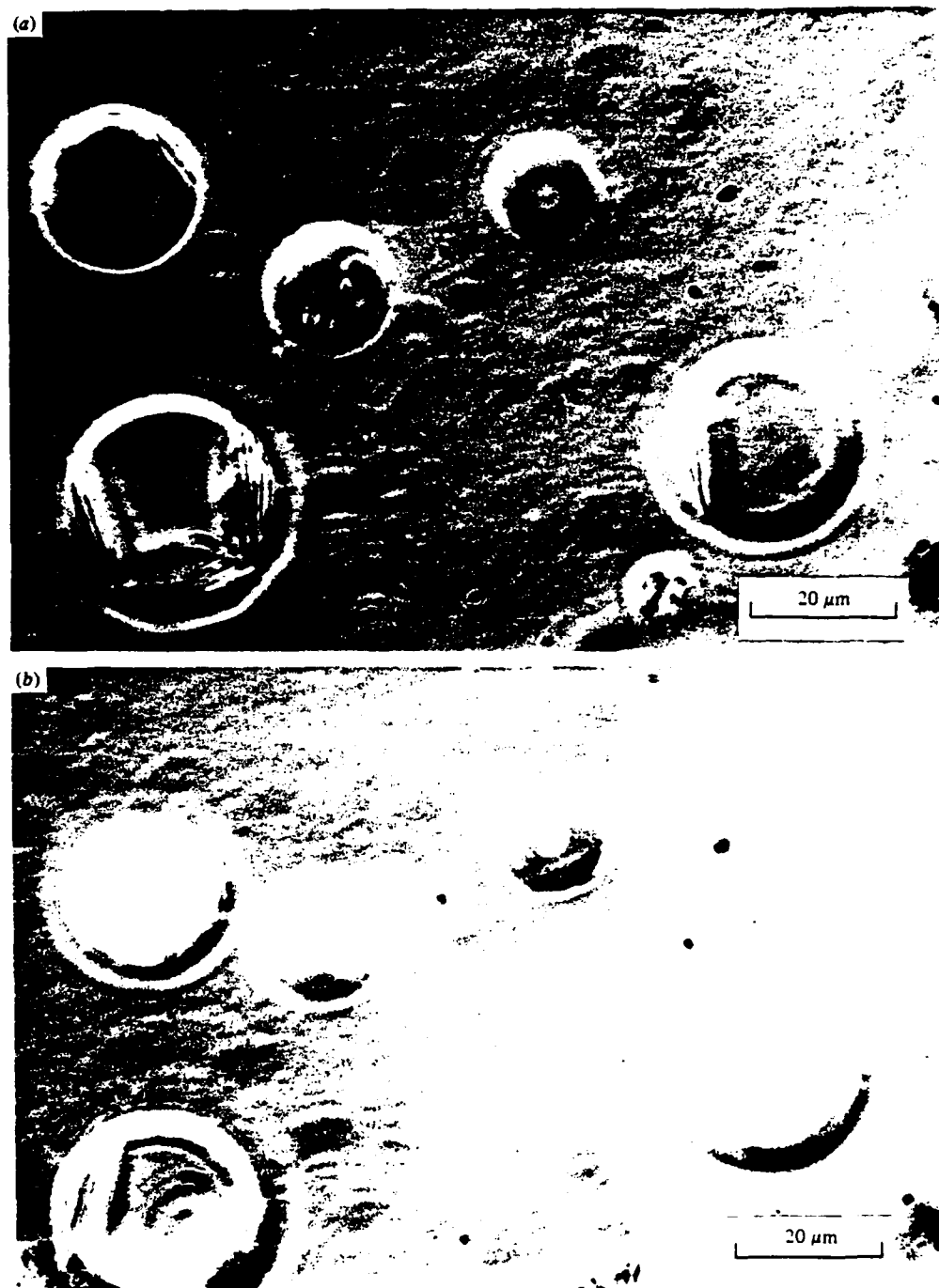


FIGURE 2. Photomicrograph of spherical plastic particles with embedded lead carbonate crystal 'mirrors', in index-matching fluid, by phase-contrast microscopy. (a) Transmitted light, (b) reflected light.

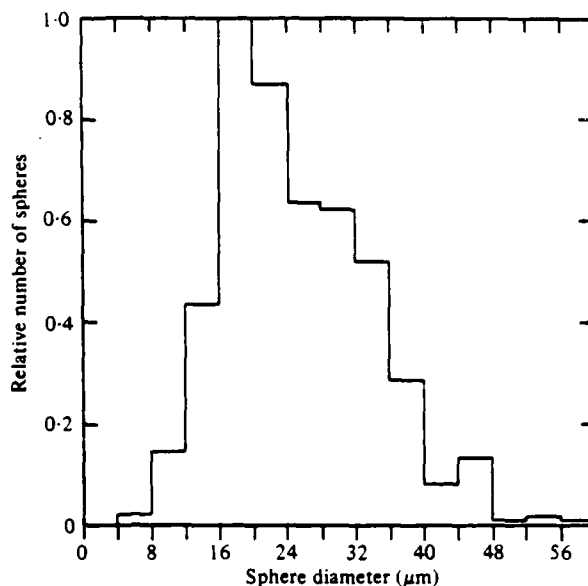


FIGURE 3. Histogram of particle diameter distribution.

reflexion of a laser beam from a mirror-bearing sphere rotates with angular velocity equal to the local vorticity  $\omega$ .

The following subsections describe the manufacture and characteristics of the probe particles.

#### (a) Particle manufacture

Methylmethacrylate monomer, a volatile, low-viscosity liquid, is easily 'mass' polymerized (Rodriguez 1970; Redfarn & Bedford 1960) by adding a small amount (0.1% by weight) of initiator (usually benzoyl peroxide) and heating for several hours. A clear, hard, plastic solid (commercially known as Lucite or Plexiglas) results. If the non-water-soluble monomer is suspended in a continuously stirred aqueous solution, it breaks up into small spherical 'pearls' and the same chemical polymerization occurs. This procedure is known as suspension or pearl polymerization since the pearls retain their shape when hardened.

The suspension fluid consists of 2 g/l polyvinyl alcohol (PVA), 1.5 g/l each of sodium chloride (NaCl) and ammonium thiocyanate ( $\text{NH}_4\text{SCN}$ ) in doubly distilled water. PVA prevents the liquid pearls from coalescing once they are separated, NaCl helps to prevent partially polymerized pearls from sticking together, and  $\text{NH}_4\text{SCN}$  inhibits the formation of emulsion polymer (Rodriguez 1970; Hopff, Lüssi & Gerspacher 1964). Approximately 150 ml of monomer plus initiator is added to 850 ml of solution, and then whipped for 5 s in a Montgomery Ward pulse action blender. The suspension is then poured into a one-litre volumetric flask, heated to 65–70°C and magnetically stirred on a Corning heater/stirrer for about five hours. The spheres harden and, when, dried form about 100 ml of slippery powder.

Lead carbonate 'mirrors' are easily incorporated in the particles before they



polymerize by adding 7.5 ml of Mearlmaid Nacromer ZTX-B (supplied by Mearl Co.) to the monomer before whipping. The mirrors are hexagonal platelets with widths of 8–30  $\mu\text{m}$ , thickness of 0.07  $\mu\text{m}$  and refractive index of 2.2 (see figure 1). The mirrors generally remain fully enclosed by the plastic spheres throughout the process and do not interfere with the polymerization chemistry.

#### (b) Particle characteristics

The resulting spheres have a density of about 1.2  $\text{g cm}^{-3}$  and a refractive index of 1.49. Microscopy shows a diameter range of about 5–200  $\mu\text{m}$ . The smallest spheres contain no mirrors, the larger ones contain several. Since only spheres smaller than a Kolmogorov microscale (Tennekes & Lumley 1972) of roughly 50  $\mu\text{m}$  that contain mirrors are desired, gravitational sedimentation (Cadle 1955) is used to narrow the size range. Figures 2(a, b) show phase-contrast photomicrographs of finished particles imbedded in an index-matching fluid and illuminated by transmitted and reflected light respectively. Measurements of many similar pictures determined the final particle diameter distribution shown in figure 3. The average diameter is 21  $\mu\text{m}$ . It appears that there are on the average about two mirrors per sphere.

To check for flocculation and non-spherical or otherwise defective particles a microscopic flow system was constructed in which the particles could be observed under actual flow conditions. It was found that a small minimum shear rate, which is easily surpassed in any laboratory flow system, sufficed to keep the spheres dispersed. The observations also show that approximately 3 % of the particles have defects such as fractures or non-spherical form. An additional 3–4 % appear to be stuck together in inseparable pairs or occasional triplets.

#### 2.3. Fluid selection

The particles must be suspended in a fluid having the following properties: (1) refractive index which nearly matches that of the spheres (1.49) to prevent scattering from their surfaces that would limit the optical depth; (2) no dissolution or chemical reactivity with the particles or components of the flow system; (3) density near that of the particles to prevent rapid settling out; (4) low viscosity to facilitate experiments with high Reynolds number; (5) non-foaming surface properties; (6) low vapour pressure, toxicity and flammability for safety and convenience; and (7) low cost to permit economical extension to large-scale apparatus.

Two fluids, dibutyl phthalate and *p*-cymene, were found which satisfy all or most of the requirements. The former has a viscosity of 0.15  $\text{g cm}^{-1} \text{s}^{-1}$  which is suitable for the laminar flow experiments, while the latter has lower viscosity, 0.005  $\text{g cm}^{-1} \text{s}^{-1}$ , but somewhat higher flammability and vapour pressure. Certain concentrated solutions of salts in water that also satisfy most of these criteria are excessively corrosive.

#### 2.4. Detection system

The detection system consists of two parts, the optical system and the electronics for data collection and processing. The optical system is designed to perform two functions: Define the sampled volume in the fluid, and define the particle rotation angle to be timed by the electronics. The sampled volume is defined by the illuminating laser beam and a lens-slit combination that collects the reflections and limits the observed

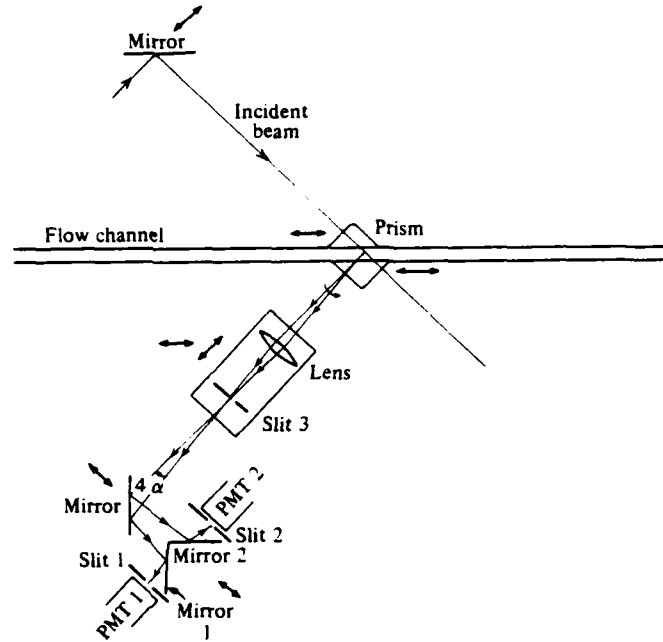


FIGURE 4. Optical detection system.

length of the laser beam as will be described. Another pair of slits with fixed separation defines the rotation angle. Light passing through these slits is converted to electrical pulses by photomultipliers (RCA 7265). The pulses trigger a pair of threshold detectors, one of which (*on*) starts a clock on a pulse from the first PMT and the second (*off*) stops the clock on a pulse from the second PMT. The elapsed time is read by a computer which immediately calculates the vorticity. The accuracy of the data is determined by the regularity of the light beams passing through the slits, which in turn is determined by the quality of the reflexions from the particles and the quality of the optical components. In this section the detection system is described in detail to provide a basis for a determination of the measurement uncertainty function.

#### (a) Optical system

(i) *Optical system geometry.* Figure 4 shows a schematic diagram of the optical system and its relationship to the flow system. The incident beam enters the channel at a  $45^\circ$  angle through a prism which is refractive-index-matched to the channel wall. The reflexions from suitably oriented particles emerge nearly perpendicular to the incident beam through a second prism and are imaged without magnification onto slit 3, as indicated by the ray tracing in figure 4. The incident beam and slit 3 define the sampled volume. Slits 1 and 2 are fixed in position; along with movable mirrors 1 and 2 they define the particle rotation angle,  $2\alpha$ , through which a particle rotating in the direction indicated must turn for its reflexion to pass from slit 1 to slit 2. Since the reflexions rotate twice as fast as the particles, the slits define an actual angle of  $4\alpha$ . The maximum height of these slits in this apparatus is 5 cm, limited by the size of the photomultiplier

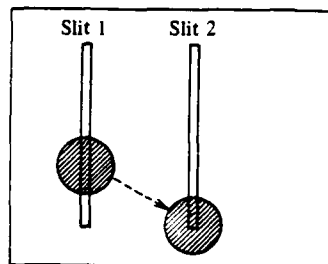


FIGURE 5. Possible positions of reflected diffraction spot relative to slits, illustrating its truncation.

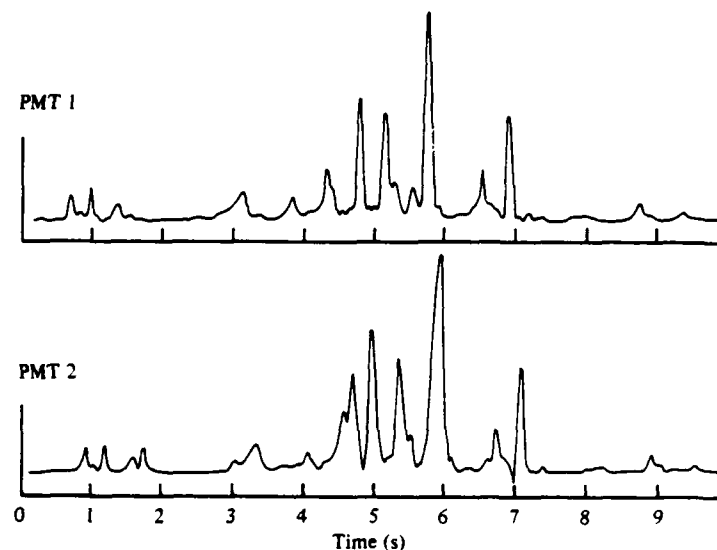


FIGURE 6. Segment of dual-channel chart recorder trace showing output of photomultipliers due to reflexions from particles embedded in a rigidly rotating rod.

anodes placed directly behind them. Consequently, only about 4% of the total number of reflexions are intercepted by the optics. A more elaborate apparatus with specially shaped slits and larger detectors could increase the collection efficiency substantially. All of the optical components are movable, as shown by the double-headed arrows in figure 4, to allow repositioning of the sampled volume without significantly changing the reflexion path length of 37 cm or the rotation angle  $2\alpha$ .

(ii) *Properties of the reflexions.* Reflexions of parallel illumination from perfect mirrors, approximated by disks of radius  $L$ , are diffraction broadened to Airy disk patterns with the central disk spreading at an angle  $\beta = 1.22\lambda/2L$ . For the probe mirrors  $\beta \sim 1.5^\circ$ . For an incident beam intensity  $I$ , the reflected power is  $I\pi L^2$ . The observed irradiance on a plane a distance  $z$  from the mirror is

$$I_r = I\pi L^2 / [\pi(\beta z)^2] = 2.69IL^4/\lambda^2 z^2. \quad (2.6)$$

Thus the intensity of the reflexion varies with the fourth power of mirror size. Additional variations can arise from the following factors: (1) particles move through an incident

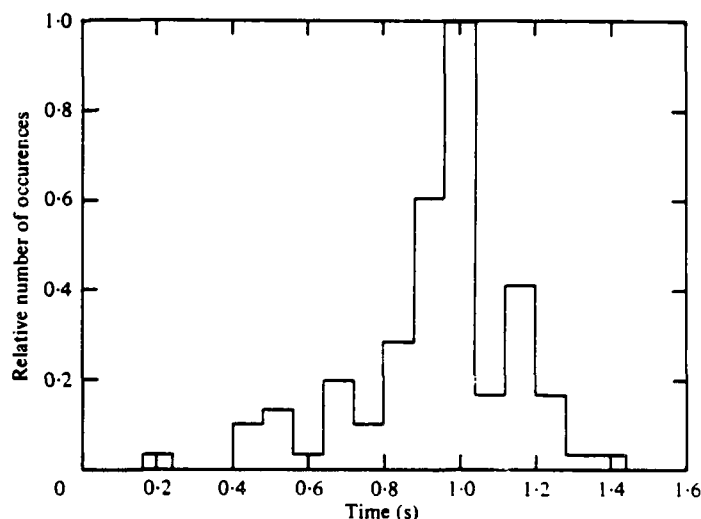


FIGURE 7. Distribution of elapsed times between threshold crossings of detector 1 followed by detector 2, as determined from data like that of figure 6.

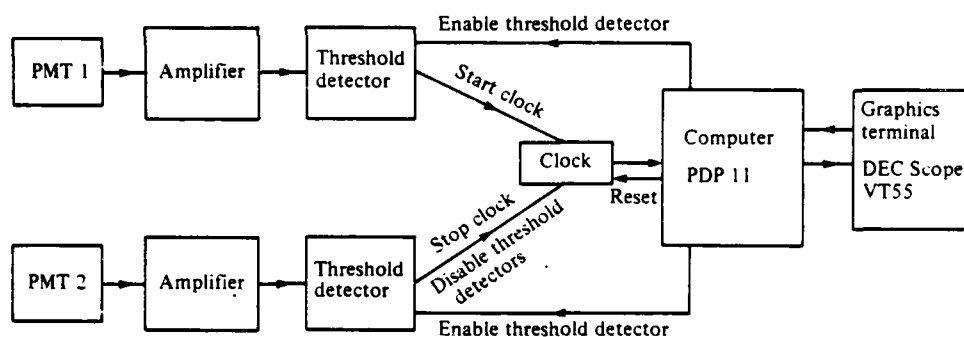


FIGURE 8. Block diagram of data analysis system.

beam with a gaussian intensity profile while they rotate, thus changing reflexion intensity; (2) as shown in figure 5, portions of the reflected beam may be cut off by the top or bottom of a slit; (3) the intensity of the ideal reflexions is angle dependent; (4) mirror imperfections as well as differences in mirror diameter vary the intensity between particles; and (5) optical screening by separate particles can attenuate the reflexion.

To characterize the reflexions a dummy specimen consisting of particles imbedded in a rigid rod of polymethylmethacrylate was rotated in the illuminating beam at one revolution per minute. Figure 6 is a segment of a dual-channel chart recorder trace of the output of the two photomultipliers recording these reflexions. The upper trace is PMT1 and the lower is PMT2. Examination of this figure shows that the amplitude and shapes of pulses from different particles can vary substantially, and frequently the individual pulses comprising a pair differ from each other.

As shown in appendix A, the result of these variations is an uncertainty in the

measurement time between the pulses detected using a threshold detection criterion. This 'pulse variation' error can be minimized by maximizing the separation in time of the two pulses relative to their width, that is by maximizing the rotation angle  $\alpha$  and minimizing the diffraction width  $\beta$ , or maximizing the ratio  $\alpha/\beta$ . A narrow pulse width is achieved by the use of a short wavelength of light, for which a He-Cd laser (Liconix Model 401,  $\lambda = 4431 \text{ \AA}$ ) was chosen. The optimum rotation angle is difficult to determine because all of the deleterious variations become more pronounced as the rotation angle increases and disappear at zero rotation angle. Thus there is a trade-off between maximum time separation and minimum shape variation. In practice choosing  $\alpha/\beta \sim 1$  proved to be satisfactory. The measured elapsed time distribution for a constant rotation rate of the dummy specimen is plotted in figure 7. This distribution eventually determines the vorticity measurement resolution to be discussed in § 3.

#### (b) Electronics

A block diagram of the data acquisition system is shown in figure 8. Threshold detectors are employed to determine the time of occurrence of the pulses. A pulse from PMT1, after amplification, triggers a threshold detector, starting a clock which is accurate to  $1 \mu\text{s}$ . A similar event in the second channel stops the clock and disables the threshold detectors. The elapsed time is read by an on-line computer which then resets the clock and threshold detectors, and subsequently operates on the data. To suppress low-vorticity noise, discussed in § 3 below, the system automatically resets after a predetermined elapsed time if no pulse is presented to the *off* detector. The data are converted to vorticity in the computer and displayed on a graphics terminal. Note that measurements of vorticity of only one algebraic sign are recorded with this system as described. Both signs could, however, be simultaneously recorded with duplicate electronics in which the *on* and *off* channels are interchanged.

### 3. Analysis of system characteristics

The precision and accuracy of vorticity measurement, data acquisition rate, temporal resolution, spatial resolution associated with the fluid volume sampled, and the background noise spectrum characterize the vorticity measurement system. These properties are closely interrelated and may be optimized selectively to suit various applications.

A special requirement of the optimization procedure is the selection of conditions that facilitate convenient separation of the measured vorticity spectrum from the characteristic background noise of the VOP system, which is unique in that the noise spectrum depends on the vorticity (signal) spectrum as well as instrumental parameters. Below, in § 3.1, expressions describing the data rate and spatial and temporal resolutions are derived, the background noise is discussed in detail, and a simple demonstration of the optimization technique is presented.

Section 3.2 describes the experimental resolution which can be expected after optimization. A system resolution function combining the effects of flow inhomogeneities and optical variations is developed to facilitate analysis of experimental results.

## 3.1. Data rate and noise analysis

(a) *Data rate.* Assume a sampled volume of cross-sectional area  $A$  and uniform length  $s$ , a mirror concentration  $n$ , flow at mean velocity  $v$ , and a vorticity vector  $(\omega_1, 0, 0)$ . The rate at which mirrors enter and pass through the sampled volume is  $nAv$ , of which a small fraction,  $f$ , will present the proper vertical orientation to reflect light in the direction of slits 1 and 2, which are positioned to measure the  $x$  component of vorticity. Thus the effective mirror passage rate is  $R_p = nAvf$ . The particles rotate through an angle  $\phi = \frac{1}{2}(s/v)\omega_1$  while they transit the sample volume. Those that rotate through the appropriate azimuth defined by slit 1 and continue through an additional angle  $2\alpha$  before leaving the sampled volume can generate vorticity data.

The temporal resolution associated with an individual datum is the time for rotation through  $2\alpha$ , that is  $\tau_1 = 4\alpha/\omega_1$ . Ideally  $\alpha \rightarrow 0$  would yield instantaneous data. In this limit the probability of a mirror entering the sampled volume with an initial azimuth suitable for data production is  $\phi/2\pi$ , yielding an ideal limiting data rate  $R_i = 2R_p\phi/2\pi$  (see appendix B), or

$$R_i = fnAs\omega_1/2\pi = fN\omega_1/2\pi, \quad (3.1)$$

where  $N$  is the average number of mirrors within the sampled volume.  $R_i$  is also the limiting data rate generated by a mirror density  $n$  as the flow velocity vanishes, or  $\phi \rightarrow \infty$ . The mirrors rotate at a frequency  $\omega_1/4\pi$  with a fraction  $f$  oriented to produce two data per rotation, due to the twofold symmetry of the mirrors.

To measure a rotation time the detector slits 1 and 2 must be separated; hence  $\alpha$  is necessarily non-zero. Consequently, at non-zero flow velocity, some mirrors enter the sampled volume with an azimuth which will not allow data generation during their residence time. A mirror may then generate pulses which either trigger the *on* detector and the *off* detector in sequence, producing a 'valid' datum, trigger only one detector, or trigger no detector before leaving the sampled volume. Appendix B enumerates these possibilities and shows that mirrors having an initial azimuth suitable for valid data production are detected at a rate

$$\left. \begin{aligned} R_a &= fnAv(\phi - 2\alpha)/\pi, & (\phi - 2\alpha) > 0, \\ R_a &= 0, & (\phi - 2\alpha) < 0. \end{aligned} \right\} \quad (3.2)$$

The rate at which the individual detectors are triggered, however, remains equal to  $R_i$ , independent of  $\alpha$  and  $v$ . The difference,  $R_r = R_i - R_a$ , defines the rate at which pulses appear in each detection channel that have no correlated pulses (those due to the same reflexion) in the other channel. These 'random' pulses result in a further reduction of the measured data rate by occasionally appearing between the two correlated or 'valid' pulses comprising the 'valid on-off pair' required to generate a valid datum. Random pulses occurring sequentially in the two channels may also produce 'false' data values, resulting in 'background noise'.

The measured valid data rate,  $R_m$ , is determined by enumeration of the possible sequences of events involving valid and random pulses. Five such sequences can occur:

- (1) A valid on-off pair is uninterrupted and produces a valid datum.
- (2) A valid pulse starts the clock and a random pulse stops it, generating noise.
- (3) A random pulse starts the clock and a valid off pulse stops it, generating noise and disqualifying the valid pair from data production.
- (4) Random pulses both start and stop the clock, generating noise.

(5) Two (or more) valid on-off pairs overlap, disqualifying the second pair from data production.

Sequences 2, 3 and 5 limit the measured data rate to some value less than  $R_a$ . In addition, sequences 2, 3 and 4 generate invalid elapsed-time measurements, thus creating a spectrum of false vorticity noise.

The measured data rate then is

$$R_m = R_a - R_2 - R_3 - R_5, \quad (3.3)$$

where  $R_j$  are the rates at which the enumerated sequences  $j = 2, 3, 5$  occur. These rates are calculated in appendix C with the results

$$R_2 = R_a[1 - \exp(-4\alpha R_r/\omega_1)], \quad (3.4a)$$

$$R_3 = R_a R_r/(R_r + R_i), \quad (3.4b)$$

$$R_5 = R_a[1 - \exp(-4\alpha R_a/\omega_1)]. \quad (3.4c)$$

On inserting these results in (3.3), the measured data rate becomes

$$R_m = R_a[\exp(-4\alpha R_r/\omega_1) + \exp(-4\alpha R_a/\omega_1) - (2R_r + R_i)/(R_r + R_i)]. \quad (3.5)$$

(b) *Noise.* Sequences 2, 3 and 4 above yield continuous distributions of values of the elapsed time. Since these are all Poisson processes (appendix C), the probability density of elapsed times is directly calculable. Weighting the probability densities with the corresponding noise generation rates yields the total elapsed-time noise distribution:

$$D_n(t_n) = [R_r R_i^2/(R_r + R_i)] \exp(-R_i t_n) + \begin{cases} R_a R_r \exp(-R_r t_n), & t_n < 4\alpha/\omega_1, \\ 0, & t_n > 4\alpha/\omega_1. \end{cases} \quad (3.6)$$

The first term is generated by sequences 3 and 4, and the second term is by sequence 2. This distribution determines a fictitious vorticity distribution, or vorticity noise spectrum, conveniently written as

$$B_n(\omega_n) = [4\alpha(R_i - R_a)/\omega_n^2] [\exp(-4\alpha R_i/\omega_n)] \times [R_i^2/(2R_i - R_a) + \begin{cases} R_a \exp(4\alpha R_a/\omega_n), & \omega_n > \omega_1, \\ 0, & \omega_n < \omega_1. \end{cases}] \quad (3.7)$$

This distribution has a sharp peak at  $\omega_n(\text{peak}) = 2\alpha R_i$ , and a long tail towards high values of vorticity. The total noise data rate is

$$R_n = (R_i^2 + R_i R_a - R_a^2)/(2R_i - R_a) - R_a \exp[-4\alpha(R_i - R_a)/\omega_1]. \quad (3.8)$$

(c) *Discussion and optimization.* The measured data rate given by (3.5) is implicitly a function of all experimental parameters,  $R_m = R_m(f, N, \alpha, s, v, \omega_1)$ . The VOP system is optimized by maximizing the data rate for a particular experimental vorticity value and spatial resolution. The spatial resolution  $s^{-1}$  is limited by the requirement that the mirrors have sufficient residence time in the sampled volume to rotate through the mirror  $2\alpha$  before translating out of the sampled volume, that is,  $R_a \geq 0$ , or by (3.2)

$$\omega_1/v \geq 4\alpha/s. \quad (3.9)$$

The data rate is limited by overlapping pulse pairs if the flow velocity is small, and by the requirement that the true vorticity peak be easily distinguished from the noise spectrum if operating near the vorticity/velocity threshold limit given by (3.9). Since both the data rate and the noise spectrum depend on the number of mirrors within the sampled volume, optimization generally imposes a condition on  $N$ . Examination of equations (3.5) and (3.7) in the limits  $v \rightarrow 0$  and  $\omega_1/v \rightarrow 4\alpha/s$  illustrate these limitations.

(i) *Zero flow velocity limit.* Since  $R_r \rightarrow 0$  and  $R_a \rightarrow R_i$  as  $v \rightarrow 0$ , (3.5) shows that

$$\lim_{v \rightarrow 0} R_m = R_i \exp(-4\alpha R_i/\omega_1). \quad (3.10)$$

This data measurement rate peaks at  $R_i = \omega_1/4\alpha$ , resulting in a maximum possible data rate of

$$R_{m \max} = \omega_1/4e\alpha = \omega_1/10.87\alpha. \quad (3.11)$$

Optimization of the number of mirrors in the sampled volume for this data rate requires, from (3.1),

$$N_{\text{opt}} = \pi/2fe\alpha = 0.58/f\alpha. \quad (3.12)$$

Either more or fewer mirrors in the sampled volume will reduce the data rate.

(ii) *Vorticity threshold limit.* In the vorticity measurement threshold limit,  $\omega_1/v \rightarrow 4\alpha/s$ , the valid pulse pair rate  $R_a \rightarrow 0$  and  $R_n \rightarrow R_i$ , so that all of the pulses eventually become random, and the vorticity peak vanishes into the noise background. Appropriate approximations of (3.5) and (3.7) provide an analysis of the approach to this limit.

The background noise spectrum at  $\omega_n = \omega_1$  here becomes

$$B_n(\omega_1) \simeq 2\alpha R_i^2/\omega_1^2 = \frac{1}{2}\alpha(fN/\pi)^2, \quad (3.13)$$

where the assumption  $2fN\alpha/\pi \ll 1$  has been invoked to approximate the exponential in (3.7) by unity. Equation (3.5) becomes, approximately,

$$R_m \simeq (fN/2\pi)(\omega_1/2 - 2\alpha v/s). \quad (3.14)$$

Assuming that the valid data peak at  $\omega_1$  is actually spread over a width  $\delta\omega$ , the spectral density of the valid data is  $R_m/\delta\omega$  so that a 'signal to noise' ratio can be defined as

$$r_n = (R_m/\delta\omega)/B_n(\omega_1) = \pi(\omega_1/2 - 2\alpha v/s)/\alpha f N \delta\omega. \quad (3.15)$$

Selection of a signal-to-noise ratio  $r_n$  as large as desired specifies a maximum value of  $N$ ,

$$N \leq \pi(\omega_1/2 - 2\alpha v/s)/\alpha f r_n \delta\omega. \quad (3.16)$$

With the maximum value of  $N$ , the noise peak occurs at

$$\omega_n(\text{peak}) = 2\alpha R_i = \omega_1(\omega_1/2 - 2\alpha v/s)/r_n \delta\omega. \quad (3.17)$$

If  $\omega_1/\delta\omega \ll 1$  then  $\omega_n(\text{peak}) \ll \omega_1$  and the false peak is clearly separated from the real peak, as desired. These results are graphically illustrated in figure 9 where the valid peak is represented by a gaussian of width  $\delta\omega$ ,  $r_n = 20$ ,  $N$  is determined by (3.15) and the other experimental parameters are chosen to correspond to actual experiments.

(iii) *General case.* The entire discussion of data rate and noise has, to this point, assumed a single value (or narrow range) of the vorticity vector, enabling this comprehensive illustration of optimization. However, real flow fields may have a distribution of vorticity vectors spread out in magnitude and containing components other than the one which is sampled. In such situations the values of  $R_i$  and  $R_a$  are still proportional to the mirror density  $n$ , but quantitative analysis becomes excessively tedious. However, the preceding discussion suggests that the true vorticity spectrum can always be separated from the noise spectrum by reducing the particle concentration until the peak of the noise spectrum is located at a value of vorticity which is much



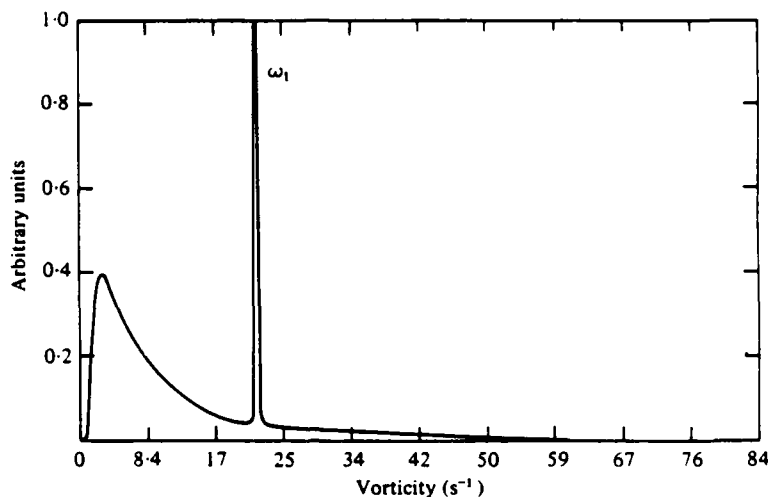


FIGURE 9. Theoretical noise distribution near vorticity/velocity threshold value.

less than the threshold value of measurable vorticity,  $\omega_{min}$ , for the particular flow situation. This peak is easily recognized but it can be suppressed by automatically resetting the detectors after a time interval  $t_r$  has elapsed after an *on* pulse without an *off* pulse. Choosing  $t_r$  so that  $4\alpha/\omega_{min} \leq t_r \leq 1/R_i$  allows a slight increase in the measured data rate, and a considerable improvement in the appearance of the vorticity distribution by suppressing the low-vorticity noise.

### 3.2. Vorticity resolution

Vorticity measurement uncertainties limit the vorticity resolution of the VOP system and broaden measurements of vorticity distributions. Limitations of optical geometry and imperfection of the probe particle reflexions introduce small errors in all reflexion transit time measurements and thus in vorticity measurements, whatever the flow system. In addition finite spatial resolution in the presence of a macroscopic spatial vorticity gradient broadens the vorticity distribution. In order to describe the properties of the VOP system, a vorticity resolution function is defined. It consists of a convolution of an optical resolution function  $g_o$  and a function  $g_v$  due to vorticity gradients. The contribution of noise is ignored in the theoretical analysis presented here.

#### (a) Optical resolution

An experimental estimate of the optical resolution in the absence of a vorticity gradient is obtainable from the simulation vortex experiment described in § 2.4 (a) (ii). The measured time delay distribution shown in figure 7 can be inverted to obtain the measured optical resolution shown in figure 10. This experiment determines the optical resolution function  $g_o(\omega/\omega_1)$  of the present VOP system for a vorticity spike at  $\omega_1$ . It displays a smooth optical resolution function peak with a root-mean-square vorticity resolution of about 9 %. Since this experiment suffers from a small vorticity/velocity ratio away from the axis of rotation, it is not surprising that a broad low-level tail at higher vorticity appears. It is a combination of the pulse variation error

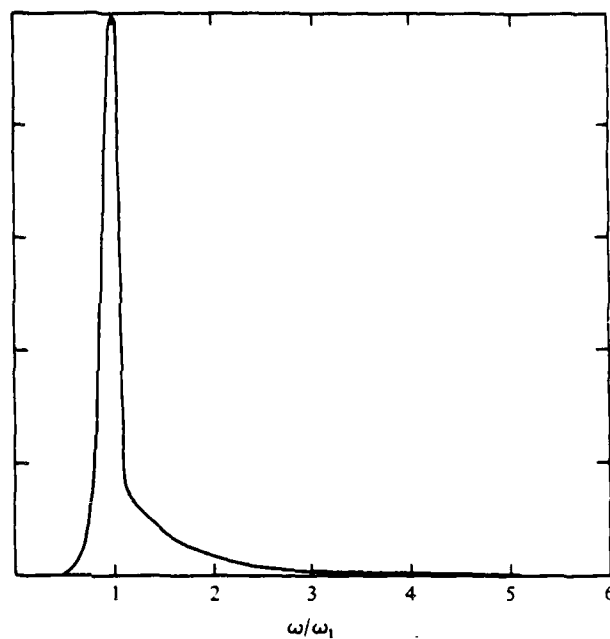


FIGURE 10. Experimentally determined optical resolution function.

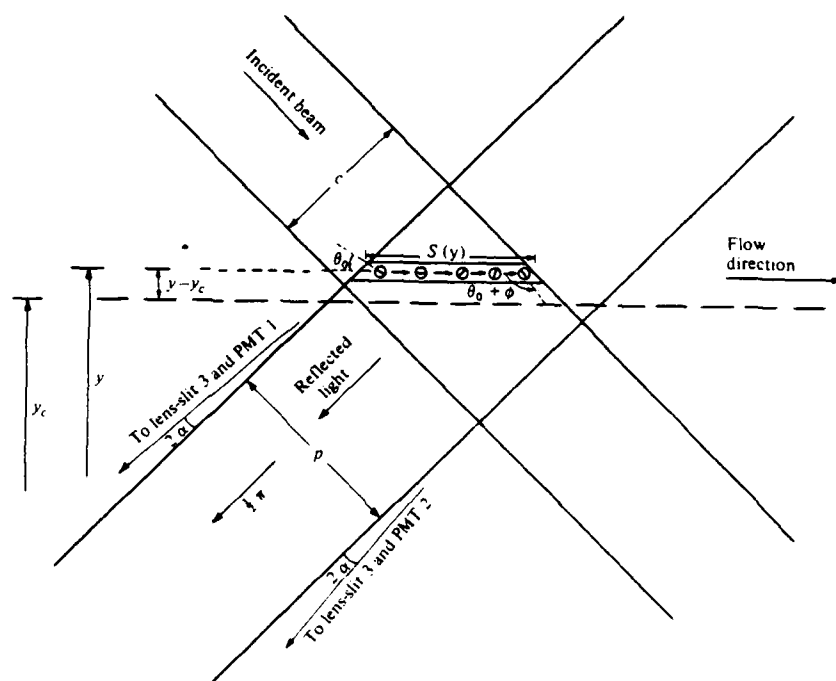


FIGURE 11. Notation for analysis of sampled volume.

Limits (valid for $y > 0, d > c$ )	$s(y)$
$(d-c)/2\sqrt{2} > (y-y_c) > -(d-c)/2\sqrt{2}$	$\sqrt{(2)} c$
$(d+c)/2\sqrt{2} > (y-y_c) > (d-c)/2\sqrt{2}$	$\sqrt{(2)} c - 2[y-y_c - (d-c)/2\sqrt{2}]$
$-(d+c)/2\sqrt{2} < (y-y_c) < (d-c)/2\sqrt{2}$	$\sqrt{(2)} c + 2[y-y_c + (d-c)/2\sqrt{2}]$

TABLE 1

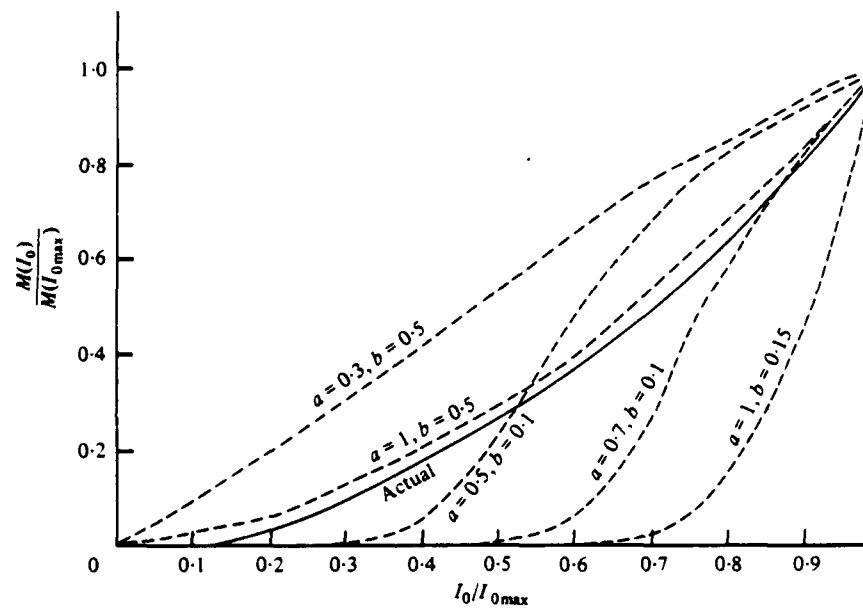


FIGURE 12. Theoretical and experimental pulse detection rates as a function of intensity, used to determine the reflexion intensity distribution.

discussed in appendix A and the false data background discussed in the previous section. Note that the pulse variation error, as well as the noise, increases in magnitude as  $\phi \rightarrow 2\alpha$  since the particles translate through a larger segment of the gaussian incident intensity profile. This means that the accuracy of the data improves as  $\omega/v$  increases, and that the relative magnitude of the tail will depend on  $\omega/v$ .

#### (b) Vorticity gradient resolution

The measured vorticity distribution in a system with non-uniform vorticity is determined primarily by the size and shape of the sampled volume, and the vorticity and velocity gradients. For the optical geometry shown in figure 11 the sampled volume is a rectangular box oriented at  $45^\circ$  relative to a flow channel. The length  $s$  varies with position. Calling  $y$  the co-ordinate relative to the centre of the channel and  $y_c$  the position of the centre of the sampled volume relative to the centre of the flow channel, then the length at position  $y$ ,  $s(y, y_c, c, d)$  has the values summarized in table 1, where  $c$  is the width of the incident beam and  $d$  the width of slit 3. The local contribution to

the data rate, now a function of  $y$ , is approximated by (3.2) with the assumption that the effects of random pulses and overlapping valid pulse pairs are negligible. Thus

$$R_a = R_a[\phi(\omega(y, y_c), v(y, y_c), s(y, y_c, c, d))] = fnAv(\phi - 2\alpha)/\pi, \quad \phi > 2\alpha, \quad (3.18)$$

where the function  $\phi(\omega)$  is the angle through which a particle rotates during its transit of the sampled volume, defined in §3.1 (a). A measurement of vorticity with the sampled volume centred at point  $y_c$  will now result in a vorticity distribution  $g_v(\omega, v, c, d)$ , where  $g_v \propto R_a$ . This piece of the resolution function is called the vorticity-sampling function.

(c) *Optically corrected sampling function*

The non-uniformity of the illuminating laser beam and the distribution of probe particle reflecting power couple in a curious fashion. The illumination is non-uniform because the laser beam has a gaussian intensity profile. Since larger probe mirrors reflect more strongly than small mirrors they trigger the threshold reflexion detectors at lower illumination intensities and thus are observable farther out into the fringes of the illuminating beam.

Defining  $m(I)dI$  as the number of additional reflexions that will become detectable as the incident intensity increases from  $I$  to  $I+dI$ , the total number of mirrors with reflexions bright enough to be detectable is  $\int_0^{I_0} m(I)dI$  if the maximum incident intensity is  $I_0$ . Defining the intensity-dependent beam width,  $c = c(I)$ , the number of single channel reflexions detected per unit time is

$$M = B \int_0^{I_0} c(I) m(I) dI, \quad (3.19)$$

where  $B$  is some constant. For a gaussian laser beam of width  $c_0$  at  $I/I_0 = e^{-2}$  the beam width between points of intensity  $I$  is  $c(I)/c_0 = (\frac{1}{2} \ln(I_0/I))^{\frac{1}{2}}$  so that

$$M(I_0) = c_0 B \int_0^{I_0} (\frac{1}{2} \ln(I_0/I))^{\frac{1}{2}} m(I) dI. \quad (3.20)$$

Fitting  $m(I)$  to a gaussian function for simplicity yields

$$M(I_0) = c_0 B \int_0^{I_0} (\frac{1}{2} \ln(I_0/I))^{\frac{1}{2}} \exp[-(I/I_0 - a)^2/2b^2] dI. \quad (3.21)$$

Figure 12 shows several scaled curves of  $M(I_0)$  vs.  $I_0$  with various values of  $a$  and  $b$ . Actual data, obtained by counting the number of pulses triggering threshold detector 1 in a fixed period of time for various attenuations of the incident beam, most closely fits the curve with  $a = 1$ ,  $b = 0.5$ . The vorticity gradient function  $g_v$  can now be adjusted to  $g'_v(\omega, y_c, c_0, d)$  to account for the variations in probe particle reflecting power by performing the integral

$$g'_v(\omega, y_c, c_0, d) = \int_0^{I_0} g_v[\omega, y_c, c(I), d] m(I) dI. \quad (3.22)$$

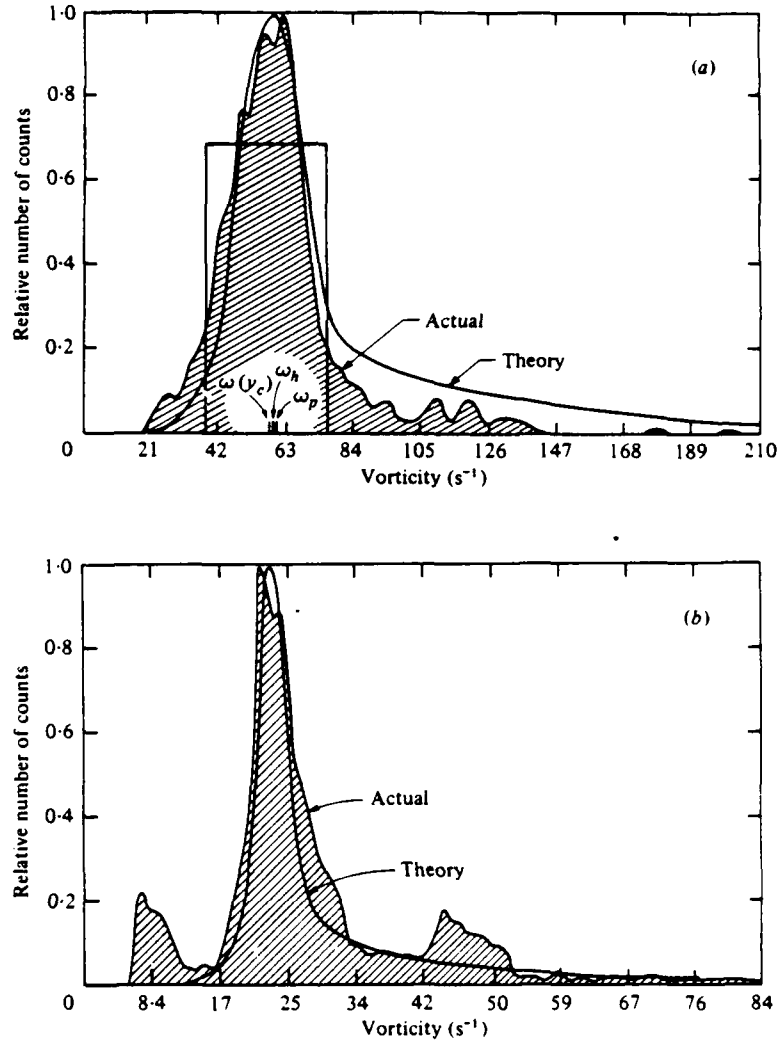


FIGURE 13. Superposition of vorticity resolution function and measured distribution. Flow parameters: (a)  $w = 0.22$  cm,  $y_c = 0.157$  cm,  $c_0 = 0.1$  cm,  $d = 0.1$  cm,  $v_0 = 8.65$  cm s $^{-1}$ , (b)  $w = 0.8$  cm,  $y_c = 0.74$  cm,  $c_0 = 0.1$  cm,  $d = 0.1$  cm,  $v_0 = 10.3$  cm s $^{-1}$ .

(d) *Vorticity resolution function*

The complete vorticity resolution function  $g(\omega, y_c, c_0, d)$  is the convolution of the corrected sampling function  $g'_c$  with the measured optical resolution function  $g_o$ . Thus the vorticity resolution function is

$$\left. \begin{aligned} g(\omega, y_c, c_0, d) &= \int_0^\infty d\omega_a g'_c(\omega_a, y_c, c_0, d) g_o(\omega/\omega_a) \\ &= \int_0^\infty d\omega_a g_o(\omega/\omega_a) \int_0^{I_0} dI g_r(\omega_a, y_c, c(I), d) \exp[-2(I/I_0 - 1)^2] \end{aligned} \right\} \quad (3.23)$$

(e) *Illustrative calculation of vorticity resolution function*

The simple example of laminar two-dimensional, Poiseuille flow (Batchelor 1967, § 4.2) illustrates the calculation of the vorticity resolution function. The velocity and vorticity profiles are for this case

$$v(y) = v_0(1 - y^2/w^2), \quad \omega(y) = 2v_0y/w^2, \quad (3.24), (3.25)$$

where  $v_0$  is the velocity at the centre of the channel and  $w$  is the channel width. The angle of particle rotation during transit of the sampled volume is

$$\phi(y, y_c, c, d) = s(y, y_c, c, d)y/(w^2 - y^2). \quad (3.26)$$

The local data rate within the sampled volume is

$$R_a = (fnv_0h dy/\pi)(1 - y^2/w^2)[sy/(w^2 - y^2) - 2\alpha], \quad (3.27)$$

where  $h dy$  is the cross-sectional area. Treating  $y$  as a function of vorticity, the vorticity-sampling function is

$$g_v(\omega, y_c, c, d) = s[y(\omega), y_c, c, d]y(\omega) - 2\alpha[w^2 - y^2(\omega)]. \quad (3.28)$$

Now the vorticity resolution function  $g(\omega, y_c, c, d)$  can be calculated since all of its components are determined. The bold lines in figures 13(a, b) show the results of numerical calculations of  $g(\omega(v_0, w), y_c, c_0, d)$  from (3.22) for the present VOP system with the parameters  $v_0, w, y_c, c_0$  and  $d$  indicated in the figure caption. For this high-symmetry geometry ( $c_0 \simeq d$ ) the vorticity distribution is nearly symmetric, except for the noise tail. Therefore several convenient measures of the position of the vorticity peak nearly coincide, namely the putative vorticity at the centre of the measuring volume  $\omega(y_c)$ , the peak vorticity  $\omega_p$ , and the mean of the half-maximum points  $\omega_h$ .

#### 4. VOP system test

##### 4.1. Test system

Laminar, two-dimensional Poiseuille flow provides a suitable, stringent test of the reliability of the new vorticity measurement system. A Plexiglas channel, 5.1 cm high, 1.3 cm wide, and 50 cm long was constructed for this purpose. An extra piece of Plexiglas, 5.1 cm high and 25 cm long, can be inserted to reduce the channel width to a nominal 0.4 cm. A gravity-fed, recirculating pumping system drives the fluid, dibutyl phthalate, through the free-surfaced channel. Screens placed in the entrance region smooth out gross flow irregularities. Flow velocity maxima were determined by measuring the transit times of visible particles between fiducial marks. The flow system has provisions to vary all of the parameters entering into the resolution function of § 3, to facilitate its use for testing and calibrating the VOP system and determining its vorticity resolutions. A cylindrical lens placed in the path of the incident beam can change the otherwise cylindrical sampled volume into a rectangular parallelepiped.

Flow visualization was used to determine the areas within the channel where the flow is sufficiently well developed for good measurements. Suspended guanine platelets (Kalliroscope Corporation product AQ-1000) are aligned by the flow in the direction of the maximum shear rate, making boundary layers and flow inhomogeneities clearly visible. The velocity and vorticity profiles become fully developed slightly downstream

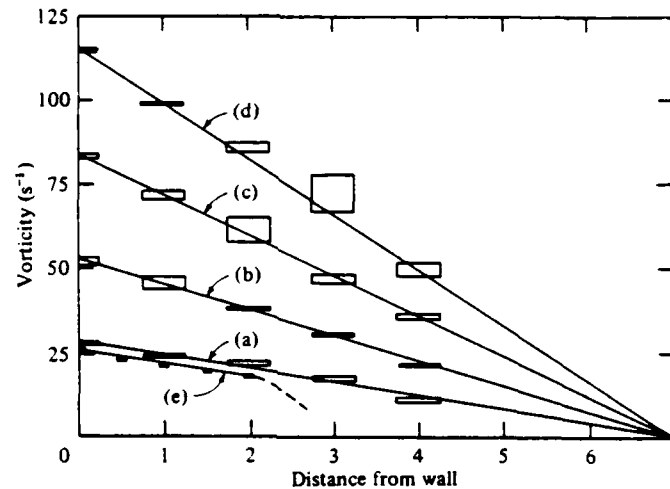


FIGURE 14. Measured vorticity profiles in Poiseuille flow. Calculated speeds: (a)  $2.9 \text{ cm s}^{-1}$ ; (b)  $4.8 \text{ cm s}^{-1}$ ; (c)  $8.6 \text{ cm s}^{-1}$ ; (d)  $13.0 \text{ cm s}^{-1}$ ; (e)  $10.3 \text{ cm s}^{-1}$ .

of the point at which the boundary layers from either side of the channel meet. In the  $0.4 \text{ cm}$  wide channel, observations show that this occurs at positions at least  $20 \text{ cm}$  downstream of the entrance. In the  $1.3 \text{ cm}$  wide channel it was not clear that the Poiseuille flow developed fully for velocities above  $3 \text{ cm s}^{-1}$ . Effects of the bottom of the channel appeared to be negligible above  $2.5 \text{ cm}$ . Velocities at the centre of the channel range from about  $1$  to  $15 \text{ cm s}^{-1}$ .

#### 4.2. Vorticity distributions

Figure 13(a) compares an anticipated vorticity distribution calculated in § 3 with the corresponding measured distribution using the same flow parameters in the narrow channel. The agreement is quite good, especially near the half-maximum points. The noise and pulse variation errors for this flow are apparently less significant than in the simulation vortex experiment of § 2.4(a)(ii), as indicated by the differences in the tail heights. Figure 13(b) shows a similar comparison of some wide-channel data taken near the channel wall. Note that the wide channel has a shallower vorticity gradient than the narrow channel, with a correspondingly narrower sampling function as expected. It also has a smaller vorticity/velocity ratio, which is responsible for the increased experimental tail amplitude and the small noise peak at low vorticity values. This distribution can be compared to the theoretical noise distribution of figure 9. The automatic reset circuit is responsible for the sharp cut-off at the low end of the experimental distribution. The experimental wide-channel data shows a curious secondary peak centred at approximately twice the value of the primary peak which appears only in observations close to the wall. It may be the result of some sort of flow fluctuations. The Reynolds number ( $v_0 w / \nu$ ) for this flow is about 100.

A numerical device which is useful to compare different vorticity distributions is demonstrated by the rectangle drawn in figure 13(a). The width and position of this rectangular construction are determined to yield the second and third moments of the

experimental distribution around its average. The bottom 10 % of the distribution is ignored in calculating the moments to eliminate the contributions of the various errors.

(a) *Vorticity profiles*

Several sets of vorticity measurements are plotted as functions of measurement position  $y_c$  in figure 14. They show, within error limits, the anticipated linear vorticity profiles for these Poiseuille flows, (3.25). Each vorticity point is plotted as a rectangle with a width representative of the positional uncertainty and a height equal to the difference between two measures of vorticity, namely the peak vorticity  $\omega_p$  and the average of the half-maxima  $\omega_h$ . In accord with § 3.2 (d),  $\omega_p$  and  $\omega_h$  should very nearly coincide with the vorticity at the centre of the sampled volume,  $\omega(y_c)$ . The experimental values of  $\omega_h$  are repeatable to within a few per cent and are thus good measures of  $\omega(y_c)$ . The r.m.s. value of the differences  $\omega_p - \omega_h$  provide a practical measure of the uncertainties of vorticity measurements. For these data the relative uncertainty of vorticity is about 8%.

The velocities indicated in figure 14 are calculated from the slopes of the straight lines determined by the vorticity measurements, since this measure is more precise than the flow velocity estimates. The calculated velocities do agree with the approximate measured velocities.

In the wide channel the flow has not reached a fully developed Poiseuille parabolic velocity profile. Boundary-layer theory (Landau & Lifshitz 1959, ch. 4) shows that the boundary layer 20 cm downstream from the edge of a flat plate will have a width of about 0.5 cm when the flow velocity is 10 cm s<sup>-1</sup> and kinematic viscosity is 0.15 cm<sup>2</sup> s<sup>-1</sup>. Thus there should be a high-vorticity boundary layer with small vorticity gradient near the wall that drops rapidly to zero near the edge of the boundary layer. The wide-channel vorticity profile, line (e) in fig. 14, appears to have a fully developed flow profile near the wall for a channel width of 1.6 cm at the correct centre-line velocity of 10.3 cm s<sup>-1</sup>. However the actual channel width is only 1.3 cm and the vorticity drops sharply below the detectable minimum beyond 0.25 cm from the wall. These results are consistent with the above calculations and with the flow visualization observations that a distinct boundary layer remains.

(b) *Distribution widths*

Poiseuille flow allows a very simple comparison to be made between the expected vorticity resolution and the actual width of the distribution. According to equation (3.25), if a width,  $\Delta y$ , of the vorticity profile is uniformly sampled ( $s = \text{constant}$ ), then the corresponding width  $\Delta\omega$  of the vorticity distribution is

$$\Delta\omega = (2v_0/w^2) \Delta y. \quad (4.1)$$

In the present experiment (4.1) should provide a reasonable approximation even though  $s$  varies. Figure 15 shows a plot of mean values of  $\Delta\omega$  for each of the lines in figure 14 vs.  $2v_0/w^2$  and a straight line fit for comparison with  $\Delta y$  determined by (4.1). Here  $\Delta\omega$  is chosen as the width of the rectangular construction discussed above. The resulting value for  $\Delta y$ ,  $\sim 0.1$  cm, agrees with the value determined by the apparatus optics.



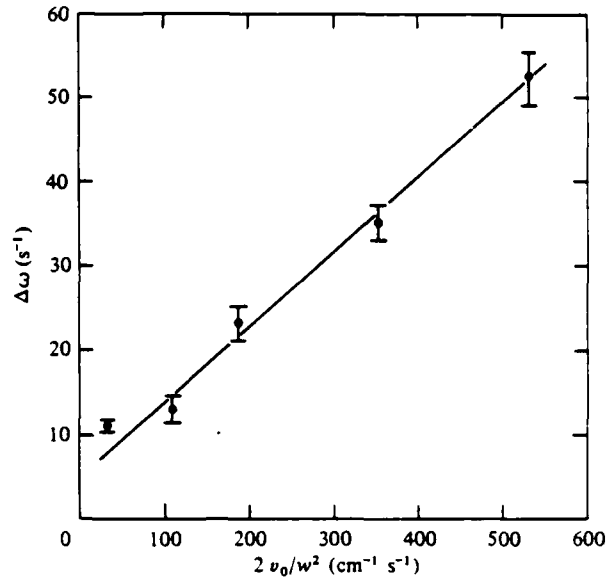


FIGURE 15. Experimental vorticity distribution widths as a function of flow parameter. Slope = 0.09 cm.

### 5. Summary

A system for vorticity measurement by direct optical probe has been described and tested under the stringent conditions imposed by laminar flows. The accuracy, vorticity resolution, data rate and spatial resolution of the VOP and the experimental parameters on which these properties depend have been analysed and demonstrated by the measurements with a rather primitive apparatus.

There are some fundamental interdependent limits on the VOP system capabilities. The drift velocity/vorticity ratio sets a lower limit on the spatial resolution,  $s_{\min} = 4\alpha v/\omega$ , since the residence time of a probe particle within the sampled volume must exceed the vorticity detection time. An upper limit on the number of particles within the sampled volume with zero flow velocity,  $N_{\text{opt}} = 0.58/f\alpha$ , is determined by maximizing the data rate while requiring that reflexions from multiple particles have a small probability of overlapping. The factor  $f$  represents the geometrical data collection efficiency, which may be improved by more elaborate optical design. The maximum data acquisition rate,  $R_{m \max} = \omega/10.87\alpha$ , is achieved in a zero flow velocity situation if the number density is determined  $N_{\text{opt}}$ . As the flow velocity increases from zero the maximum data rate decreases and background noise increases. The signal to noise ratio,  $r_n \approx \pi(\frac{1}{2}\omega - 2\alpha v/s)/\alpha f N \delta \omega$  can be made as large as desired for any value of vorticity greater than the limiting value of  $\omega = 4\alpha v/s$  by selecting a sufficiently small mirror number density, thus separating the valid data from the background. Table 2 summarizes this discussion of limiting-system capabilities and gives the parameters of the present realization of the VOP system.

The discussion of the background noise reveals one noteworthy point. As  $\alpha \rightarrow 0$  all noise disappears, the particle number density is limited only by the size of the spherical

Parameter	Typical value
(A) Spatial resolution $s_{\min} = 4\alpha v/\omega$	$\alpha = 0.05$ $s_{\min} = \begin{cases} 200 \mu & (v/\omega = 0.1 \text{ cm}) \\ 900 \mu & (v/\omega = 0.5 \text{ cm}) \end{cases}$
(B) Data rate	
(1) Maximum $R_{\max} = \omega/10.87\alpha$	$R_{\max} = 1.84\omega$
(2) Actual	
(a) Zero flow velocity $R_i = \frac{1}{2}\omega (fN/\pi)$	$N = 10$ $f = 0.04$ $R_i = \omega/16$
(b) Near $\omega/v$ threshold $R_s = (\frac{1}{2}\omega - 2\alpha v/s) (fN/\pi)$	
(C) Signal-to-noise ratio $r_n = 2\pi(\frac{1}{2}\omega - 2\alpha v/s)/\alpha f N \delta\omega$	$\omega = 22 \text{ s}^{-1}$ $v = 10.3 \text{ cm s}^{-1}$ $\delta\omega = 10 \text{ s}^{-1}$ $r_n = 22$
(D) Vorticity resolution Present practical limit	$\sim 9\%$

TABLE 2. Present VOP system parameters.

probe particles, and the data rate is bounded by only this density limit. In the present VOP system  $\alpha$  must be non-zero to deal with variations of the size and shape of the reflexions. The rotation angle  $2\alpha$  is coupled to the divergence angle of the micro-mirror reflexions by the requirement  $\alpha/\beta \gtrsim 1$ . However, if particles with completely uniform mirrors, preferably perfect disks, could be produced, and if the illuminating beam were converted from a gaussian to a 'top-hat' intensity profile, the vorticity could be determined by measuring the width of a single pulse peak as it transits a slit. The minimum value of  $\alpha$  could then be determined by the temporal resolution of the electronics, and would be very close to zero. Since the vorticity resolution, discussed at length in §3, is also coupled to the optical parameters, the illuminating-beam intensity profile, and the particle uniformity, it would also be substantially improved by better particles. Substantial improvement of all of the operational parameters can be expected in future VOP systems. Nevertheless the need for refractive index matching of fluid and particles seems inescapable.

There appear to be no substantial obstacles to measurement of vorticity spectra and spatial correlations even in turbulence although various potential capabilities of the system, particularly those applicable to turbulence, have not yet been fully established. All three components of vorticity should be simultaneously measurable by straightforward elaboration of the present VOP system. Some special properties of the vorticity field are readily accessible since positive and negative signs of vorticity components are automatically separated. The VOP can readily average vorticity distributions over large flow volumes.

We have adapted the VOP system to vorticity measurements in mixing layers, wakes and turbulent boundary layers and are proceeding to investigate grid turbulence and coherent-structure phenomena of the type analysed in recent experimental and theoretical works (Roshko 1976; Kovasznay 1978; Aref & Siggia 1980).

We gratefully acknowledge stimulating conversations with Gary Watson, Jerry Gollub, Eric Siggia, Hassan Aref, Mark Nelkin and Spahr Webb, guidance in the assembly of the mini-computer system by Jerry Gollub, initiation into the mysteries of pearl polymerization by F. Rodriguez and patient and persistent craft in the production and evaluation of the probe particles by Chad Arnold. This work was partially supported by the National Science Foundation Grant NDR-77-0031.

### Appendix A

Consider the measurement of the time interval between two roughly gaussian-shaped pulses which may have truncated or very noisy tops. The noise prevents the use of a peak detector as an accurate indicator of the occurrence of an event. A threshold detector may provide more reliable data, but introduces errors if the pulse amplitudes and widths are not constant.

Assume the pulses have Gaussian shape but different width and height, with their peaks separated by a true time  $\tau_p$ . The pulses are described by the equations

$$S_1(t) = A_1 \exp[-t^2/2\sigma_1^2], \quad (\text{A } 1)$$

$$S_2(t) = A_2 \exp[(t - \tau_p)^2/2\sigma_2^2]. \quad (\text{A } 2)$$

If the threshold detectors trigger at an amplitude  $a_0$  the measured elapsed time is  $\tau = t_2 - t_1 = \tau_p + \sigma_1(2 \ln A_1)^{1/2} - \sigma_2(2 \ln A_2)^{1/2}$ . The fractional error is

$$\frac{\Delta\tau}{\tau_p} = \frac{\tau - \tau_p}{\tau_p} = \frac{\sigma_1(2 \ln A_1)^{1/2} - \sigma_2(2 \ln A_2)^{1/2}}{\tau_p}. \quad (\text{A } 3)$$

The error is minimized by maximizing  $\tau_p$  and minimizing  $\sigma_1$  and  $\sigma_2$ . If  $\sigma_1 \approx \sigma_2$  and  $A_1 = CA_2$ , where  $C$  is a constant, then  $\Delta\tau \approx \sigma_2\sqrt{(2)}[(\ln C + \ln A_2)^{1/2} - (\ln A_2)^{1/2}]$ , which approaches zero as  $A_2$  increases, suggesting that large pulse amplitudes are also desirable.

### Appendix B

Here are derived the rates of registry of valid vorticity data and of false data due to velocity-induced rapid transits of the sampled volume, and the resulting false vorticity distribution.

Defining a co-ordinate system for mirror orientation in which the azimuthal direction to the point half-way between slits 1 and 2 is taken as  $\frac{1}{2}\pi$ , a mirror enters the sampled volume with azimuth  $\theta_0$  and exits at azimuth  $\theta = \theta_0 + \phi$ , where  $\phi = \frac{1}{2}(s/v)\omega$ . To register a valid vorticity datum it must pass through azimuths  $\frac{1}{2}\pi - \alpha$  and then  $\frac{1}{2}\pi + \alpha$  to trigger PMT1 (*on*) and PMT2 (*off*) in sequence (see figure 11). While traversing the sampled

Probability	$\phi < 2\alpha$	$2\alpha < \phi < 2\pi - 2\alpha$	$2\pi - 2\alpha < \phi < 2\pi$	$2\pi < \phi < 2\pi + 2\alpha$	$\phi > 2\pi + 2\alpha$
$P_a$	0	$\frac{\phi - 2\alpha}{2\pi}$	$\frac{\phi - 2\alpha}{2\pi}$	0†	†
$P_b$	$\phi/2\pi$	$\frac{2\alpha}{2\pi}$	$\frac{2\pi - \phi}{2\pi}$	0	†
$P_c$	$\phi/2\pi$	$\frac{2\alpha}{2\pi}$	$\frac{2\pi - \phi}{2\pi}$	0	†
$P_d$	$\frac{2\pi - 2\phi}{2\pi}$	$\frac{2\pi - 2\alpha - \phi}{2\pi}$	0	0	†
$P_e$	0	0	$\frac{2\alpha + \phi - 2\pi}{2\pi}$	$\frac{2\alpha - \phi + 2\pi}{2\pi}$	†
$P_{a+c}$	0	0	0	$\frac{\phi - 2\pi}{2\pi}$	†
$P_{b+c}$	0	0	0	$\frac{\phi - 2\pi}{2\pi}$	†
$P_{a+d}$	0	0	0	$\frac{4\pi - \phi - 2\alpha}{2\pi}$	†

† When  $\phi > 2\pi + 2\alpha$  substitute  $\phi - 2j\pi$  for  $\phi$ , where  $j$  is the integer indicating the number of complete revolutions that have occurred:  $j$  type- $a$  events and one additional event must occur for each particle.

‡ Note that  $P_{a+c} + P_{b+c} + P_{a+d} = (\phi + 2\alpha)/2\pi$ .

TABLE 3

volume a single rotating mirror with  $\phi < 2\pi$ , referred to below as an event, can trigger the detectors in several possible sequences, generating the following five distinct cases.

Event	Result
(a) $\theta_0 < \frac{1}{2}\pi - \alpha$ , $\theta > \frac{1}{2}\pi + \alpha$	good data
(b) $\theta_0 > \frac{1}{2}\pi - \alpha$ , $\theta > \frac{1}{2}\pi + \alpha$	off only
(c) $\theta_0 < \frac{1}{2}\pi - \alpha$ , $\theta < \frac{1}{2}\pi + \alpha$	on only
(d) $\theta < \frac{1}{2}\pi - \alpha$	no detection
(e) $\theta_0 < \frac{1}{2}\pi + \alpha$ , $\theta > \frac{1}{2}\pi - \alpha$	off followed by on

If  $\phi > 2\pi$  then each mirror can generate more than one event. Table 3 shows the probability of occurrences of each type of event generated by an individual mirror.  $P_x$  denotes the probability of only a type  $x$  event, while  $P_{x+y}$  denotes the joint probability of a type  $x$  event followed by a type  $y$  event.

The average rate at which type  $x$  events occur is equal to twice the mean rate ( $R_p = fNAv$ ) at which mirrors with proper (detectable) vertical orientation flow through the sample volume times the event probability  $P_x$ ,

$$R_x = 2R_p P_x, \quad (\text{B } 1)$$

except that type  $a$  events (valid data generators) occur at the rate  $R_a = 2(k + P_a) R_p$ , where the integer  $k$  is the number of complete rotations. The factor of 2 is a result of the rotational symmetry of the mirrors. Of interest are the observations that, for all  $\phi > 2\alpha$ ,  $R_a = R_p(\phi - 2\alpha)/2\pi$ , and the rates at which all *on* (type  $a$  or  $c$  or  $e$ ) and all *off* (type  $a$  or  $b$  or  $e$ ) events occur equal, not surprisingly, the ideal data rate, or

$$R_{on} = R_{off} = R_i = fN\omega/2\pi.$$

### Appendix C

The noise generation rates due to the various sequences of presentations of random and valid pulses are calculated here. Recall that pulses presented to the *off* detector before the clock has been started pass undetected. Similarly, pulses presented to the *on* detector while the clock is running also pass undetected.

Consider those sequences wherein random pulses presented to the *on* detector with rate  $R_r$  start the clock, and either random or valid pulses presented to the *off* detector at rate  $R_i$  stop it. The rate  $R_f$  of occurrence of false data generating pulse pairs in this case is the rate of random pulse presentations to the *on* detector,  $R_r$ , multiplied by the probability of detection of these pulses,  $1/(1 + R_r/R_i)$ , or

$$R_f = R_r R_i / (R_i + R_r). \quad (C 1)$$

This case can be divided into two sub-cases where the *off* detector is triggered by a valid pulse, or it is triggered by a random pulse. The first has a probability  $R_a/R_i$  of occurrence, and the second has probability  $R_r/R_i$ . Hence, the rate of random-*ons* + valid-*offs* (sequence 3) is

$$R_3 = (R_a/R_i) R_f = R_r R_a / (R_r + R_i) \quad (C 2)$$

and the rate of random-*ons*-random-*offs* (sequence 4) is

$$R_4 = R_r^2 / (R_r + R_i). \quad (C 3)$$

Random events occurring at an average rate  $R$  describe a Poisson process (Lindgren 1976). Thus, starting at an *on* detection, the normalized probability density of elapsed times until a random *off* detection is

$$P(R, t) = R \exp(-Rt), \quad (C 4)$$

where the *off* detections occur at rate  $R$ . For the cases considered above the *off* rate is, from (3.1),  $R_i$ , so  $R = R_i$ . The resulting elapsed time distribution, weighted by the false data rate, is  $D(t) = R_f P(R_i, t)$ .

Now consider sequence 2 where a valid pulse pair starts the clock and a random pulse stops it. There is an additional restriction: the random pulses must occur in the time interval  $[0, 4\alpha/\omega_1]$ . Thus the probability of this sequence occurring is

$$P_2 = \int_0^{4\alpha/\omega_1} P(R_r, t) dt = 1 - \exp(-4\alpha R_r / \omega_1). \quad (C 5)$$

Since valid pulse pairs occur at rate  $R_a$ , the rate at which this source of false data is generated is

$$R_2 = R_a P_2 = R_a [1 - \exp(-4\alpha R_r / \omega_1)]. \quad (C 6)$$

Finally, the probability of two valid pulse pairs overlapping (sequence 5) is

$$P_5 = \int_0^{4\alpha/\omega_1} P(R_a, t) dt \quad (C 7)$$

and the rate at which data is lost to this sequence of events is

$$R_5 = R_a P_5 = R_a [1 - \exp(-4\alpha R_a / \omega_1)]. \quad (C 8)$$

## REFERENCES

- AREF, H. & SIGGIA, E. D. 1980 Vortex dynamics of the two-dimensional turbulent shear layer. *J. Fluid Mech.* **100**, 705.
- BATCHELOR, G. K. 1967 *An Introduction to Fluid Dynamics*. Cambridge University Press.
- CADLE, R. 1955 *Particle Size Determination*. Wiley-Interscience.
- CHWANG, A. & WU, T. 1974 Hydromechanics of low-Reynolds-number flow. Part 1. Rotation of axisymmetric prolate bodies. *J. Fluid Mech.* **63**, 607.
- ECKELMANN, H., NYCHAS, S. G., BRODKEY, R. S. & WALLACE, J. M. 1977 Vorticity and turbulence production in pattern recognized turbulent flow structure. *Phys. Fluids* **20**, 5225.
- FOSS, J. F. 1977 The Vorcom, Part 2: Demonstration vorticity measurements. *Third Annual Report, NASA, Langley Research Center*.
- FRENKIEL, F. N., KLEBANOFF, P. S. & HUANG, T. T. 1979 Grid turbulence in air and water. *Phys. Fluids* **22**, 1606.
- HOPFF, H., LÜSSI, H. & GERSPACHER, P. 1964 Contribution to suspension polymerization. *Makromolekulare Chemie* **78**, 24.
- JEFFREY, J. B. 1922 The motion of ellipsoidal particles immersed in a viscous fluid. *Proc. Roy. Soc. A* **102**, 161.
- JOHNSON, D. H. & WEBB, W. W. 1972 *Bull. Am. Phys. Soc.* **17**, 1084. See also Johnson, D. H. 1975 Measurement of the rate of strain tensor in a turbulent flow using light scattering from asymmetric particles. Ph.D. thesis, Cornell University.
- KOVASZNAY, L. S. G. 1978 Large scale structure in turbulence: A question or an answer? In *Structure and Mechanisms of Turbulence I* (ed. H. Fiedler). Lecture Notes in Physics, vol. 75. Springer.
- LANDAU, L. & LIFSHITZ, E. 1959 *Fluid Mechanics*. Pergamon.
- LINDGREN, B. W. 1976 *Statistical Theory*, §3.2. MacMillan.
- REDFARN & BEDFORD 1960 *Experimental Plastics: A Practical Course for Students*. Wiley-Interscience.
- RODRIGUEZ, F. 1970 *Principles of Polymer Systems*. McGraw-Hill.
- ROSEHO, A. A. 1976 Structure of turbulent shear flows: A new look. *A.I.A.A. J.* **14**, 1349.
- TENNEKES, H. & LUMLEY, J. 1972 *A First Course in Turbulence*. Massachusetts Institute of Technology Press.
- WILLMARTH, W. W. & BOGAR, T. J. 1977 Survey and new measurements of turbulent structure near the wall. *Phys. Fluids* **20**, 59.

APPENDIX B

```

C          OMEGA3 VERS. 1 DEC 87
C
C      THIS PROGRAM READS A FILE OF DIGITIZED STREAK LOCATIONS ON FILM
C      COMPUTES THETA, PHI AND ASSOCIATED COEFFICIENTS FROM X,Z PAIRS
C      COMPUTES dTHETA/dt, dPHI/dt .... ACCUMULATES SUMS, AND SOLVES
C      3x3 TO EXTRACT Wx, Wy, Wz.
C
C      IMPLICIT REAL*8 (A-H,O-Z)
C      REAL*8 PHP(20), THP(20)
C      REAL*8 SD(3), SA(5,5), W(3)
C      REAL*4 XX, ZZ
C      CHARACTER*30 FLNAME
C      PI=3.14159
C
C      LOAD DATA
C
C      WRITE(*,100)
C      READ(*,101) FLNAME
C
C      ENTER Y COORDINATE (DISTANCE TO FILM PLANE)
C
C      WRITE(*,300)
C      READ(*,301) Y
C      WRITE(*,302) Y
C      WRITE(*,398)
C      SY=1.00
C      IF(Y.LT.0.00) SY=-1.00
C      OPEN(1, FILE=FLNAME, STATUS='OLD')
C      DO 3 I=1,20
C      READ(1,200,END=4,ERR=999) XX, ZZ
C      X=XX
C      Z=ZZ
C      RF=DSQRT(X*X+Z*Z)
C      TTI=RF/DABS(Y)
C      TTR=DTAN(DASIN(1.50*DSIN(DATAN(TTI))))
C      RN=RF-0.400*(TTR-TTI)
C      X=X*RN/RF
C      Z=Z*RN/RF
C      PHP(I)=SY*PI/2.00-DATAN(X/Y)
C      THP(I)=PI/2.00-DATAN(Z/DSQRT(X*X+Y*Y))
C      WRITE(*,399) THP(I), PHP(I)
C      N=I
C      CONTINUE
C      CLOSE(UNIT=2)
C
C      INITIALIZE ARRAYS
C
C      SZ=0.00
C      DO 6 K=1,3
C      SD(K)=0.00
C      W(K)=0.00
C      DO 5 FF=K,3
C      SA(K,FF)=0.00
C      CONTINUE
C      CONTINUE
C
C      ENTER TIME INTERVAL DT
C
C      WRITE(*,400)
C      READ(*,401) DT
C      WRITE(*,402) DT

```



```

C      COMPUTE DERIVATIVES, COEFFICIENTS, AND ACCUMULATE SUMS
C
      DO 7 L=2,N-1
      DTHPDT=(THP(L+1)-THP(L-1))/(2.D0*DT)
      DFHPDT=(PHP(L+1)-PHP(L-1))/(2.D0*DT)
C
      CALL TRANS(THP(L),PHP(L),SY,A,B,C,D,E,F)
C
      S2=S2+DTHPDT*DTHPDT+DFHPDT*DFHPDT
C
      SD(1)=SD(1)+DTHPDT*A+DFHPDT*D
      SD(2)=SD(2)+DTHPDT*B+DFHPDT*E
      SD(3)=SD(3)+DTHPDT*C+DFHPDT*F
C
      SA(1,1)=SA(1,1)+A*A+D*D
      SA(1,2)=SA(1,2)+A*B+D*E
      SA(1,3)=SA(1,3)+A*C+D*F
      SA(2,2)=SA(2,2)+B*B+E*E
      SA(2,3)=SA(2,3)+B*C+E*F
      SA(3,3)=SA(3,3)+C*C+F*F
7      CONTINUE
      SS11=SA(1,1)
      SS22=SA(2,2)
      SS33=SA(3,3)
      SS13=SA(1,3)
      SS23=SA(2,3)
      SS12=SA(1,2)
C
C      ... A SYMMETRIC MATRIX
C
      SA(3,2)=SA(2,3)
      SA(3,1)=SA(1,3)
      SA(2,1)=SA(1,2)
C
      DO 20 M=1,3
20      WRITE(*,449)SD(M),SA(M,1),SA(M,2),SA(M,3)
449      FORMAT('0',1PD12.4,'>',3(1PD12.4))
      CALL MATINV(SA,3,DET)
      DO 30 M=1,3
30      WRITE(*,450)SA(M,1),SA(M,2),SA(M,3)
C
C      COMPUTE Wx,Wy,Wz
C
      DO 9 I=1,3
      DO 8 J=1,3
      W(I)=W(I)+SA(I,J)*SD(J)
8      CONTINUE
9      CONTINUE
C
C      COMPUTE CHI-SQUARE AND UNCERTAINTIES
C
      NU=2*N-7
      CHID=W(1)*W(1)*SS11+W(2)*W(2)*SS22+W(3)*W(3)*SS33
      CHIC=2.D0*(W(1)*W(3)*SS13+W(1)*W(2)*SS12+W(2)*W(3)*SS23)
      CHIY=-2.D0*(W(1)*SD(1)+W(2)*SD(2)+W(3)*SD(3))
      CHI2=(CHID+CHIC+CHIY+SS2)*NU
      WRITE(*,499)NU,CHI2
C
      DW1=DSQRT(CHI2/SS11)

```

```

      DW2=DSQRT(CHI2/SS22)
      DW3=DSQRT(CHI2/SS33)

C
      WRITE(*,500) W(1),W(2),W(3)
      WRITE(*,501) DW1,DW2,DW3
      STOP
99      WRITE(*,600)
999     WRITE(*,700)
      STOP

C
C
100     FORMAT('O  ENTER INPUT FILE NAME: ',%)
101     FORMAT(A15)
200     FORMAT(2F14.7)
300     FORMAT('O  ENTER PERPENDICULAR DISTANCE TO FILM PLANE: ',%)
301     FORMAT(D12.4)
302     FORMAT(1PD12.4)
398     FORMAT('O  THETA'      PHI')
399     FORMAT(2(1PD12.4))
400     FORMAT('O  ENTER CHOPPER PERIOD: ',%)
401     FORMAT(D12.4)
402     FORMAT(1PD12.4)
450     FORMAT('O  MATRIX INVERSE ',3(1PD12.4))
499     FORMAT('O  CHI-SQUARE PER ',I2,' DEGREES OF FREEDOM= ',1PD12.4)
500     FORMAT('O  Wz= ',1PD12.4,' Wx= ',1PD12.4,' Wy= ',1PD12.4)
501     FORMAT('O  +/- ',1PD12.4,' ',1PD12.4,' ',1PD12.4)
600     FORMAT('OPEN ERROR')
700     FORMAT('READ ERROR')
      END

```

```

C
C
C      TRANSFORM TO UNPRIMED ANGLES. COMPUTE COEFFTS.
C
SUBROUTINE TRANS(THP,PHF,SY,A,B,C,D,E,F)
  IMPLICIT REAL*8 (A-H,O-Z)
  FAC=1.DO+DSIN(THP)*DCOS(PHF)
  TH=DACOS(DCOS(THP)/DSQRT(2.DO*FAC))
  PH=SY*DACOS(FAC/DSQRT(2.DO*(FAC-DCOS(THP)*DCOS(THP)/2.DO)))

```

```

C
      STH=DSIN(TH)
      CTH=DCOS(TH)
      SPH=DSIN(PH)
      CPH=DCOS(PH)
      STHP=DSQRT(1.DO-4.DO*STH*STH*CTH*CTH*CPH*CPH)

```

```

C
C      COEFFICIENTS
C
      A=2.DO*STH*CTH*SPH/STHP
      B=-2.DO*SPH*CPH*STH*STH/STHP
      C=2.DO*(STH*STH*CPH*CPH-CTH*CTH)/STHP
      D=2.DO*STH*STH*(1.DO-2.DO*CTH*CTH*CPH*CPH)/(STHP*STHP)
      E=2.DO*STH*CTH*CPH*(1.DO-2.DO*CPH*CPH*STH*STH)/(STHP*STHP)
      F=-2.DO*STH*CTH*SPH*(1.DO+2.DO*CPH*CPH*STH*STH)/(STHP*STHP)
      RETURN
      END

```

```

C
C
C      MATRIX INVERSION ROUTINE. MATINV. FROM
      BEVINGTON,P.R., DATA REDUCTION AND ANALYSIS

```

END

DATE

FILMED

9-88

DTIC